International Journal of Heat and Mass Transfer 269 (2026) 129153

Contents lists available at ScienceDirect

International Journal of Heat and Mass Transfer

journal homepage: www.elsevier.com/locate/ijhmt

A unified fractal analytical model for spontaneous imbibition in rough porous media considering dynamic wettability and gravitational effects

Hui Yue [a], Yong Kong [a], Jos Derksen [b], Ying Li [c], Yubiao Sun [a,*]

[a] *School of Interdisciplinary Science, Beijing Institute of Technology, Beijing 100081, China*
[b] *School of Engineering, University of Aberdeen, Aberdeen AB24 3UE, UK*
[c] *Qiming Information Technology Co., Ltd., Changchun 130000, China*

ARTICLE INFO

Keywords:
Spontaneous imbibition
Dynamic contact angle
Surface roughness
Lambert W function
Multiphase flow
Multiscale modeling

ABSTRACT

Dynamic wetting on rough walls is crucial to the mass transfer mechanism of gas-liquid spontaneous imbibition in multiscale porous energy systems. However, obtaining analytical solutions for dynamic wetting in rough porous media under gravity remains challenging. In this work, we propose a novel unified mathematical model that explicitly couples the static Wenzel thermodynamic correction with the kinetic energy dissipation of the moving contact line, while systematically incorporating gravitational effects. Specifically, by introducing the Lambert W function, we transform the complex nonlinear ordinary differential equation (ODE) arising from the coupling process into a closed-form explicit analytical solution. In this model, fractal theory is applied to characterize wall roughness and facilitate macroscopic upscaling. The accuracy of the proposed model is validated against existing experimental data. Through comprehensive simulations, pore-scale control mechanisms and dimensionless scaling are investigated. The results indicate that surface roughness statically suppresses capillary forces and the equilibrium distance in micropores. Furthermore, dynamic wetting nonlinearly hinders imbibition, exponentially prolonging the equilibrium time in large pores. This effect enables intermediate pores to maintain the longest high-speed stage and the maximum dynamic contact angle. Temporally, spontaneous imbibition is sequentially governed by fractal roughness, dynamic wetting, and the Bond number. Macroscopically, multi-parameter sensitivity analysis demonstrates that neglecting dynamic wetting severely overestimates early imbibition in high-permeability media. Conversely, intrinsic viscous resistance dominates ultra-low permeability systems. Overall, this model provides an efficient analytical tool and novel physical insights into complex mass transfer processes within rough porous media.

NomenclatureLatin Symbols

A	Inner surface area of wall (m^2)
D_C	Effective diameter (m)
D_f	Pore size fractal dimension [-]
D_{fr}	Surface roughness fractal dimension [-]
g	Gravitational acceleration (m/s^2)
h	Imbibition height (m)
K	Permeability of porous media (mD)
l	Edge length of equivalent roughness element (m)
L	Length of porous media (m)
L_c	Characteristic length (m)
L_e	Effective flow length (m)
M	Imbibition volume (m^3)
N	Number of pores [-]
N_r	Number of equivalent rough cells [-]
P_d	Displacement pressure (Pa)
Q	Imbibition rate (m^3/s)
R	Pore radius / Capillary radius (m)
Re	Reynolds number [-]
S_w	Saturation [-]
t	Imbibition time (s)
v	Imbibition velocity (m/s)
x	Imbibition distance (m)
Greek Symbols	
α	Inclination angle (°)

Abbreviations: ODEs, ordinary differential equations.

* Corresponding author.

E-mail address: ybsun@bit.edu.cn (Y. Sun).

https://doi.org/10.1016/j.ijheatmasstransfer.2026.129153
Received 17 April 2026; Received in revised form 27 May 2026; Accepted 8 June 2026

β	Dynamic contact angle coefficient [-]
θ_s	Static contact angle (°)
θ_d	Dynamic contact angle (°)
θ_a	Apparent dynamic contact angle (°)
Λ	Maximum length scale for fractal scaling (m)
μ	Fluid dynamic viscosity (Pa·s)
ρ	Fluid density (kg/m^3)
σ	Interfacial tension (N/m)
τ	Tortuosity [-]
φ	Porosity [-]
Subscripts	
95%	At 95% equilibrium state
a	Apparent
avg	Average
c	Characteristic
d	Dynamic
e	Effective
max	Maximum
min	Minimum
r	Wall roughness factor
R	Rough wall
s	Static
S	Smooth wall
w	Wetting phase
Superscripts	
$*$	Dimensionless variable

1. Introduction

Gas-liquid two-phase flow in complex porous media, particularly capillary-driven spontaneous imbibition [1], represents a ubiquitous and fundamental mass transfer phenomenon bridging traditional fossil fuels and modern low-carbon energy systems [2,3]. During underground energy recovery, such as enhanced exploitation of tight/shale oil and gas [4,5] and extraction of geothermal energy [6], spontaneous imbibition governs fluid exchange efficiency between porous matrix and fracture networks. As the global energy landscape transitions toward carbon neutrality goals, the pivotal role of this microscopic physical process in the fields of renewable energy and energy storage is becoming increasingly prominent. In carbon capture, utilization, and storage [7], underground hydrogen storage engineering [8], and microscale energy conversion devices (e.g., porous materials in fuel cells) [9], transport and trapping mechanisms of gas-liquid interfaces directly dictate operational efficiency and safety of these macroscopic systems. Therefore, it is crucial to thoroughly understand the dynamics of spontaneous imbibition in complex scenarios. However, given complex microstructures and multiphase flow mechanisms in realistic porous media, developing a unified analytical prediction tool that combines high physical fidelity with computational efficiency remains a major challenge for current cross-scale simulations.

Mathematical models of capillary imbibition show great potential for predicting mass transfer dynamics in complex porous media [10,11]. The theoretical basis of existing mathematical models for imbibition in porous media can be traced back to the classical Lucas-Washburn (L-W) equation [12,13]. However, the original L-W model assumes that pores are ideal, straight circular tubes. This assumption severely limits its application in complex porous systems. To overcome this limitation, researchers have systematically extended this model over the past century by focusing on force mechanisms and geometric topology. On the one hand, subsequent models gradually incorporated fluid dynamic mechanisms, such as viscous forces [14], inertia [15], gravity [16], and buoyancy [17], into governing equations; on the other hand, later studies effectively corrected the predictive errors caused by tortuous flow paths and non-circular cross-sections in real pores by introducing tortuosity and shape factors [18–20]. Furthermore, to address the complex cross-scale pore size distributions within porous media, the introduction of fractal geometry has successfully established an analytical bridge between microscopic topological features and macroscopic multiphase flow behaviors [21,22].

However, despite their significant contributions to expanding force mechanisms and characterizing geometric topology, these studies have not yet addressed the core issue of interfacial transport in porous media, namely the thermodynamic and kinetic non-equilibrium coupling mechanisms at real gas-liquid-solid interfaces. Pore walls of real porous materials generally exhibit significant fractal roughness characteristics [23–25]. Thermodynamically, intrinsic roughness not only significantly increases microscopic flow resistance but also induces complex wetting states, such as the Wenzel state, thereby fundamentally altering the effective capillary driving force [26–28]. Furthermore, recent studies have coupled roughness with boundary slip and shape factors, revealing its significant role in modifying the spontaneous imbibition height [29,30]. Kinetically, the moving contact line induces interfacial viscous dissipation that dynamically alters the contact angle, causing a nonlinear decay in early-stage mass transfer rates [31,32]. However, current theoretical models often treat these two mechanisms separately. Few studies have explicitly coupled the roughness-induced static thermodynamic corrections and the kinetic dissipation caused by dynamic contact angles within a unified mathematical model. Lacking these fundamental interfacial physics leads to significant theoretical deviations when predicting the imbibition dynamics in porous media with pronounced roughness.

Although theoretical models can incorporate the aforementioned physical mechanisms, scaling up from microscopic pores to macroscopic cores or components still faces significant mathematical challenges [33,34]. Traditional physical experiments provide benchmark data for macroscopic transport laws, but they are time-consuming and expensive. Moreover, it is difficult to perform real-time and in-situ characterization of interfacial evolution within opaque media [35,36]. To overcome the limitations of experiments, current research has shifted toward microscopic direct simulations, such as CFD [37] or LBM [38], and pore-scale models like PNM [39] that rely on topological simplification. However, scaling these methods to macroscopic scales inevitably imposes a significant computational burden due to challenges such as large mesh counts, interface tracking, and complex nonlinear equation systems. On the other hand, macroscopic continuum models offer high computational efficiency but fail to capture microscopic nonlinearities, as they primarily depend on empirical constitutive equations [40,41]. In contrast, analytical models of capillary bundles derived from fractal geometry can achieve mathematical dimensionality reduction while preserving key physical mechanisms, making them an effective approach for cross-scale imbibition simulations [19,21]. However, when explicitly coupling thermodynamic and kinetic effects, the microscopic governing equations evolve into highly nonlinear ordinary differential equations (ODES) that are challenging to solve. Their macroscopic integration still faces the dilemma of balancing efficiency and stability, which limits their application in large-scale engineering problems.

To address the inadequate understanding of coupled physical mechanisms and the computational challenges in cross-scale modeling, this study proposes a novel unified fractal imbibition model. While previous studies have extensively utilized Lucas-Washburn-type imbibition models, fractal capillary bundle theory, Wenzel roughness correction, and dynamic contact angle correlations, the novelty of this work lies in explicitly mathematically coupling the static Wenzel thermodynamic correction with the non-equilibrium dynamic contact angle within a unified physical framework. Furthermore, instead of relying on traditional step-dependent numerical schemes, we derive a closed-form explicit analytical solution for the highly nonlinear governing equation.

Specifically, a fully coupled interfacial transport model is first established at the single-capillary scale, simultaneously incorporating wall roughness, dynamic wetting, and gravitational effects. By introducing the Lambert W function, the complex nonlinear ordinary differential equation is solved analytically. This approach effectively eliminates the truncation errors and time-step sensitivity inherent in conventional explicit Euler or implicit iterative methods. Subsequently, this pore-scale analytical solution is upscaled to macroscopic porous media using fractal capillary bundle theory and is validated against existing experimental data at both microscopic and macroscopic scales. Based on this framework, we systematically investigate the pore-scale control mechanisms, the dimensionless scaling laws of competing forces, and the macroscopic parameter sensitivity. This model provides an effective analytical tool and novel physical insights for mass transfer evaluation in complex porous energy systems.

2. Theoretical basis and model construction

Natural and engineered porous media typically feature complex structures where fluid flow is governed by the coupling of multiple physical mechanisms. To develop a unified analytical model that systematically characterizes the effects of pore structure, gravity, and apparent dynamic contact angles on spontaneous imbibition, certain simplifications of the physical processes are required. Building on established theoretical frameworks, the model is developed based on the following assumptions:

(1) The porous medium is represented as a bundle of tortuous capillaries with varying equivalent radii, where both the pore size distribution and wall roughness follow fractal scaling laws.
(2) To facilitate an analytical solution, the porous medium is assumed to be initially fully saturated with the non-wetting phase. The displacement process is idealized as piston-like, neglecting the influences of irreducible water and residual non-wetting phases.
(3) Both the wetting (liquid) and non-wetting (gas) phases are treated as incompressible Newtonian fluids, and the flow is assumed to remain in the laminar regime.
(4) Intrinsic wettability and surface tension are assumed to be uniformly distributed throughout the internal structure of the porous media.
(5) The spontaneous imbibition process is modeled as one-dimensional axial flow along the capillaries, neglecting any cross-flow between adjacent pores.
(6) The model strictly assumes the Wenzel state, where the liquid fully wets the rough pore wall and no stable trapped gas layer exists inside the roughness elements. For real porous media with Cassie-Baxter-type composite interfaces or extremely rough surfaces with air entrapment, additional corrections are required.

2.1. *Fractal characterization of rough pore surfaces and dynamic contact angle modeling*

The capillary bundle model is a widely used physical representation for describing fluid transport in microscale and nanoscale pores (Fig. 1**a**). However, real pore walls generally exhibit significant roughness features composed of protrusions and pits across multiple scales [25,27]. Previous research has demonstrated that such surface roughness is not randomly distributed but instead follows fractal scaling laws [42,43]. Therefore, fractal geometry is employed in this study to achieve a quantitative characterization of the surface (Fig. 1**b**). Assuming the rough pore surface can be covered by an infinite number of squares of varying sizes, the relationship between the covering number and the scale satisfies the following fractal equation [44]:

$$N_r = (\Lambda/l)^{D_{fr}} \tag{1}$$

where N_r is the total number of equivalent roughness elements; Λ is the maximum length scale of the fractal scaling; l is the side length of the smallest equivalent square roughness element; D_{fr} represents the fractal dimension of wall roughness, which ranges between $2 \le D_{fr} < 3$. A higher D_{fr} value indicates a more complex distribution of surface roughness. It should be noted that the fractal scale ratio Λ/l is not a universal constant but is closely related to the specific material properties and the geometric dimensions of the system. The fractal scale span of surface roughness for natural brittle rocks and porous media typically ranges from 10^2 to 10^3 [45]. Consequently, a representative baseline of $\Lambda/l = 100$ is uniformly used for subsequent macroscopic simulations.

Assuming that the side length of the squares covering the surface is sufficiently small, the local contact area with the pore wall can be approximated as a smooth plane. Consequently, the actual internal surface area A_R of the rough pore can be estimated by the product of the total number of squares N_r and the area of an individual element. By

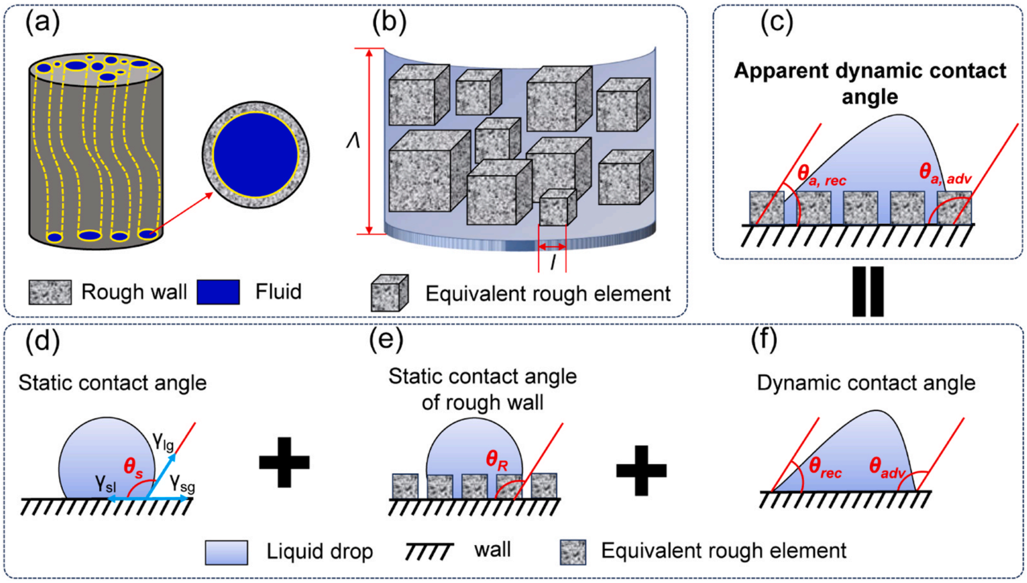

Fig. 1. Schematic of dynamic wetting mechanisms in porous media with rough surfaces. (a) Fractal tortuous capillary bundle model. (b) Equivalent micro-unit model of wall roughness. (c) Apparent dynamic contact angle. (d) Static contact angle and the three-phase contact line. (e) Static contact angle on a rough surface. (f) Dynamic contact angle.

combining this with Eq. (1), we obtain:

$$A_R = N_r l^2 = l^{2-D_{fr}} \Lambda^{D_{fr}} \tag{2}$$

According to Euclidean geometry, the fractal dimension of an absolutely smooth pore wall degenerates to its topological dimension $D_{fr} = 2$. Furthermore, the equivalent smooth pore internal surface area (A_s) can be obtained:

$$A_s = \Lambda^2 \tag{3}$$

The wall roughness factor r is defined as the ratio of the internal surface area of a rough pore A_R to that of a smooth pore A_s. Combining Eqs. (2) and (3) yields the expression for the roughness factor:

$$r = \frac{A_R}{A_s} = \left(\frac{l}{\Lambda}\right)^{2-D_{fr}} \tag{4}$$

The macroscopic contact angle θ_R on an actual rough wall and the intrinsic contact angle θ_S are illustrated in Figs. 1**(d)** and **(e)**. Under static thermodynamic equilibrium, their relationship is governed by the Wenzel equation[46]:

$$\cos\theta_R = r\cos\theta_S \tag{5}$$

However, the actual spontaneous imbibition process involves rapid movement of the gas-liquid interface, where the static thermodynamic correction in Eq. (5) alone is insufficient to describe realistic wetting dynamics. The moving three-phase contact line exhibits significant nonlinear retardation, and the dynamic contact angle depends heavily on the interface velocity (Fig. 1**f**). Based on the classical theory of non-equilibrium Young's force [31], the dynamic contact angle θ_d for a smooth wall can be expressed as:

$$\cos\theta_d = \cos\theta_S - \beta\frac{\mu}{\sigma}v \tag{6}$$

where β is the dimensionless dynamic hysteresis coefficient characterizing the viscous resistance of the moving contact line, whose value is commonly determined by conducting a linear experimental fit of macroscopic dynamic contact angle measurements against the capillary number, or theoretically evaluated by extracting the contact line friction through Molecular Dynamics simulations [47]; μ and σ are the dynamic viscosity and surface tension of the liquid, respectively. As the non-wetting phase, gas exhibits a viscosity orders of magnitude lower than that of the liquid. Thus, its viscous dissipation is neglected.

Variations in the dynamic contact angle originate from the coupling of viscous dissipation, surface topography, and intermolecular forces. Conventional models typically describe wetting dynamics solely based on interface velocity, which fails to account for the modulation of local shear stress and contact line resistance by wall roughness. To address this limitation, the apparent dynamic contact angle used in this study should be interpreted as a macroscopic-equivalent wetting parameter for rough, fully wetted pore walls [48]. Specifically, the Wenzel term represents the static thermodynamic modification of the apparent contact angle caused by the increased solid–liquid interfacial area, whereas the velocity-dependent term represents the kinetic resistance associated with the moving three-phase contact line [47,49]. Therefore, the proposed relation effectively combines the roughness-induced equilibrium wettability shift and the dynamic deviation caused by contact-line motion. Substituting the thermodynamic correction from Eq. (5) into Eq. (6) yields the predictive model for the apparent dynamic contact angle θ_a that couples these dual effects:

$$\cos\theta_a = r\cos\theta_S - \beta\frac{\mu}{\sigma}v \tag{7}$$

2.2. *Flow model in a single rough capillary under gravity*

The single-capillary model is a classic idealized representation for investigating flow processes in micro- and nanoscale pores of porous media (Fig. 2**(c)**). Fluid motion satisfies the conservation of momentum, which is generally described by the Navier-Stokes equations. For an incompressible Newtonian fluid, the momentum equation is expressed as:

$$\rho\left(\frac{\partial v}{\partial t} + \left(v\cdot\nabla v\right)\right) = -\nabla P_d + \mu\nabla^2 v + \rho g \tag{8}$$

where ρ is the fluid density; v is the velocity vector; t is time; P_d is the displacement pressure; μ is the dynamic viscosity; and g is the gravitational acceleration.

For flow in micro- and nanoscale capillaries at low Reynolds numbers ($Re \ll 1$), inertial forces are negligible. Assuming a fully developed steady laminar flow, Eq. (8) simplifies directly to the classical Poiseuille equation:

$$v = \frac{R^2 \Delta P}{8\mu x} \tag{9}$$

where, R is the capillary radius; ΔP is the total pressure drop within the tube; and x denotes the advancement distance of the gas-liquid interface. As illustrated in Fig. 2**(c)**, the total driving pressure during spontaneous imbibition in a realistic rough capillary is composed of the fractal capillary pressure, the external displacement pressure, and gravity. The governing equation for spontaneous imbibition is derived by incorporating Eq. (7) into the force balance. This equation accounts for multiple nonlinear coupling mechanisms and is expressed as:

$$v = \frac{dx}{dt} = \frac{R^2}{2\mu(4x + \beta R)}\left(\frac{2\sigma\cos\theta_s}{R}\cdot\left(\frac{l}{\Lambda}\right)^{2-D_{fr}} + \Delta P_d - \rho g x\sin\alpha\right) \tag{10}$$

where ΔP_d is the external displacement pressure; and α denotes the inclination angle of the capillary. By defining the effective imbibition height as h, the relationship between the advancement distance x and the effective height is expressed as $h = x\cdot\sin\alpha$. In particular, when the inclination angle is 90°, the imbibition height is identical to the advancement distance. Furthermore, the imbibition rate within a single capillary can be expressed as:

$$q = \pi R^2\cdot v = \frac{\pi R^4}{2\mu(4x + \beta R)}\left(\frac{2\sigma\cos\theta_s}{R}\cdot\left(\frac{l}{\Lambda}\right)^{2-D_{fr}} + \Delta P_d - \rho g x\sin\alpha\right) \tag{11}$$

To simplify the governing equation for analytical derivation, four composite parameters (A, B, C, and D) with distinct physical meanings are introduced: A characterizes the intrinsic viscous resistance; B denotes the additional resistance induced by the dynamic contact angle; C represents the total driving force; and D accounts for the gravitational resistance. Their explicit expressions are detailed in Eq. (12). This simplification effectively depicts the dynamic evolution of the fluid as it overcomes multiple resistances to reach mechanical equilibrium.

$$\begin{cases} A = \dfrac{8\mu}{R^2} \\ B = \dfrac{2\mu\beta}{R} \\ C = \dfrac{2\sigma\cos\theta_s}{R}\cdot\left(\dfrac{l}{\Lambda}\right)^{2-D_{fr}} + \Delta P_d \\ D = \rho g\sin\alpha \end{cases} \tag{12}$$

Substituting Eq. (12) into Eq. (10) simplifies the governing equation for SI as follows:

$$v = \frac{dx}{dt} = \frac{C - Dx}{Ax + B} \tag{13}$$

When $v = 0$, the equilibrium imbibition distance x_{eq} for a single capillary is determined from Eq. (13):

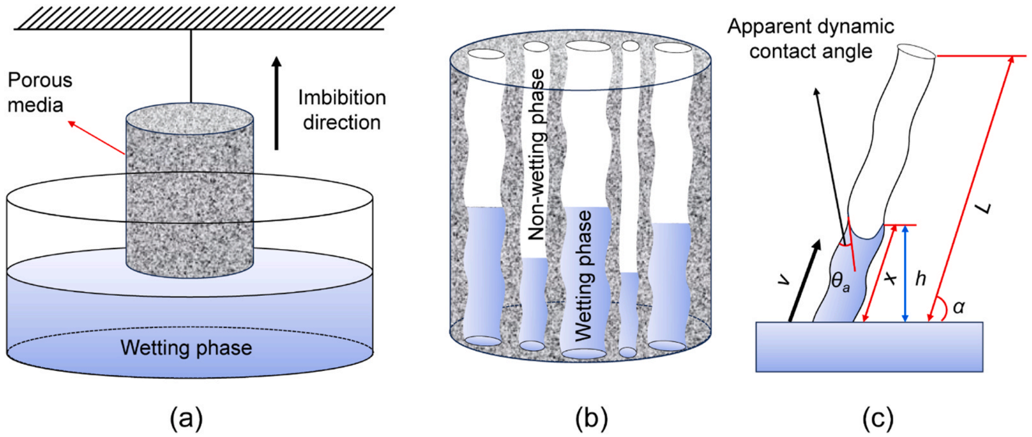

Fig. 2. Schematic of gas-liquid two-phase imbibition in porous media. (a) Real porous medium. (b) Equivalent tortuous fractal capillary bundle model. (c) Imbibition in a single rough tortuous capillary.

$$x_{eq} = \frac{C}{D} = \frac{\frac{2\sigma\ \cos\ \theta_s}{R}\cdot\left(\frac{l}{\Lambda}\right)^{2-D_f} + \Delta \mathrm{P}_d}{\rho g \sin \alpha} \tag{14}$$

Integrating Eq. (13) with the initial condition ($x = 0$, at $t = 0$) yields the implicit solution for the temporal evolution of the imbibition distance:

$$t = -\frac{A}{D}x - \frac{BD + AC}{D^2}\ln\left(1 - \frac{D}{C}x\right) \tag{15}$$

The incorporation of complex force mechanisms renders the governing equation (Eq. 13) highly nonlinear. Consequently, as shown in Eq. (15), due to the coexistence of linear and logarithmic terms, integrating this equation only yields an implicit relationship ($t = f(x)$). It is worth noting that a similar implicit analytical relationship expressing time as a function of capillary height, incorporating the gravitational effect, was previously derived and experimentally verified in sandstone by Tsunazawa et al.[50]. However, this implicit relationship is often inadequate, because extracting displacement requires expensive iterative calculations at each time step. This solution approach poses a major challenge for macroscopic engineering simulations. To ensure high computational efficiency, an explicit mathematical expression ($x = f(t)$) is essential. Therefore, to balance numerical stability and computational cost, a hierarchical solution framework comprising three strategies is established:

2.2.1. Lambert W function analytical method

By employing variable substitution, the original governing equation is recast into the standard form of the Lambert W function, $W(z)e^{W(z)} = z$. Building upon this, the explicit analytical solution for the highly nonlinear differential equation is derived, as shown in Eq. (16).

$$x(t) = \frac{C + \frac{K}{A}W\left(-\frac{AC}{K}\exp\left(-\frac{tD^2+AC}{K}\right)\right)}{D} \tag{16}$$

where $K = AC + BD$. This analytical expression provides explicit analytical solution in continuous space through a remarkably concise algebraic form, effectively eliminating the step-size constraints associated with explicit schemes and the risk of divergence inherent in implicit numerical methods.

2.2.2. Numerical iteration of implicit equations

Based on the implicit solution obtained from exact integration, a time residual function $F(x)$ is further constructed:

$$F(x) = t - \left[\frac{AC + BD}{D^2}\ln\left(\frac{C}{C - Dx}\right) - \frac{A}{D}x\right] = 0 \tag{17}$$

Subsequently, the bisection method is employed for root-finding within the valid physical interval $[0, C/D)$ (C/D denotes the theoretical maximum equilibrium distance). Although this implicit scheme is unconditionally stable, its computational efficiency is constrained by tolerance criteria and inevitably introduces numerical iteration errors.

2.2.3. Explicit Euler numerical integration

Based on the theory of time discretization, the explicit Euler scheme is utilized to discretize the differential equation directly into a recursive approximate solution:

$$x_{n+1} = x_n + \Delta t\cdot\frac{C - Dx_n}{Ax_n + B} \tag{18}$$

This approach avoids internal iteration processes and enables extremely rapid single-step computation. However, it relies heavily on infinitesimal time steps Δt to maintain numerical stability, which makes it prone to the accumulation of truncation errors or even numerical divergence.

In summary, these three categories of methods form a comprehensive solution framework across the dimensions of theoretical accuracy, numerical stability, and computational efficiency, providing diverse options for analyzing imbibition processes in various application scenarios. Specifically, the Lambert W analytical solution provides a rigorous theoretical benchmark, implicit iteration ensures numerical reliability, and the explicit Euler scheme offers a minimalist step-wise prediction. Detailed comparisons of algorithm performance are presented in Section 3.1.

2.3. Fractal capillary bundle model for spontaneous imbibition in porous media

Fig. 2**(a)** illustrates the displacement of a non-wetting phase (gas) by a wetting phase (water) in saturated porous media through spontaneous imbibition. To upscale microscopic single-capillary dynamics to a macroscopic system, the porous medium is represented as an equivalent bundle of rough tortuous capillaries (Fig. 2**(b)**). Previous studies have demonstrated that the relationship between the pore size and the cumulative number of pores in porous media follows the fractal scaling law [51]:

$$N(\xi > R) = (R_{\max}/R)^{D_f} \tag{19}$$

where $N(\xi > R)$ is the number of pores with a size greater than R; $R_{\max}$ is the maximum pore radius; D_f is the fractal dimension for pore distribution. The fractal dimension is calculated as follows [51]:

$$D_f = d - \frac{\ln \varphi}{\ln(R_{\min}/R_{\max})} \tag{20}$$

where d is the Euclidean topological dimension ($d = 2$ and $d = 3$ for two- and three-dimensional spaces, respectively); φ the effective porosity of the porous medium; $R_{\min}$ is the minimum pore radius.

Based on fractal theory, when the pore size on the cross-section of the porous medium falls within the differential interval $[R,\ R + dR]$, the differential distribution function for the number of equivalent capillaries is expressed as [16]:

$$-dN = \frac{(2 - D_f)\phi D_C{}^2}{4\left(1 - \phi\right)R_{\max}^{2-D_f}} R^{-(D_f+1)} dR \tag{21}$$

where D_C is the characteristic cross-sectional diameter or equivalent side length of the macroscopic representative elementary volume.

However, actual flow paths within real porous media are rarely straight because tortuosity effects are widespread. The tortuosity τ is defined as the ratio of the actual flow path length L_e to the macroscopic length L of the porous medium. To characterize this macroscopic geometric feature, Wang et al. [52] proposed an analytical model for the average tortuosity.

$$\tau = \frac{\left(1 - \phi\right)R_{\max}^{2-D_f}}{R_{\max}^{2-D_f} - R_{\min}^{2-D_f}} \tag{22}$$

Accounting for the influence of tortuosity, Li et al. refined Eq. (21) to derive the differential distribution function for the number of capillaries coupled with tortuosity [53]:

$$-dN = \frac{D_C{}^2}{4\tau R_{\max}^{2-D_f}} \frac{(2 - D_f)\phi}{1 - \left(\frac{R_{\min}}{R_{\max}}\right)^{2-D_f}} R^{-(D_f+1)} dR \tag{23}$$

Based on the aforementioned single-capillary fluid dynamics and fractal characteristics of porous media, the total imbibition rate of the macroscopic porous medium is determined by continuous integration of the microscopic single-capillary rate over the global pore size interval $[R_{\min},\ R_{\max}]$:

$$Q(t) = -\int_{R_{\min}}^{R_{\max}} q dN = -\frac{D_C{}^2}{4\tau R_{\max}^{2-D_f}} \frac{(2 - D_f)\phi}{1 - \left(\frac{R_{\min}}{R_{\max}}\right)^{2-D_f}} \int_{R_{\min}}^{R_{\max}} \pi R^2 \cdot v \cdot R^{-(D_f+1)} dR \tag{24}$$

Similarly, the instantaneous imbibition volume of a single microscopic capillary is defined as $m = \pi R^2 x$. The analytical expression for the macroscopic cumulative total imbibition volume is obtained through integration over the full pore size interval.

$$\begin{aligned} M(t) &= -\int_{R_{\min}}^{R_{\max}} m dN \\ &= -\frac{D_C{}^2}{4\tau R_{\max}^{2-D_f}} \frac{(2 - D_f)\phi}{1 - \left(\frac{R_{\min}}{R_{\max}}\right)^{2-D_f}} \int_{R_{\min}}^{R_{\max}} \pi R^2 \cdot x \cdot R^{-(D_f+1)} dR \end{aligned} \tag{25}$$

Based on Eq. (25), the macroscopic instantaneous wetting phase saturation of the porous medium is further calculated.

$$S_w(t) = \frac{M(t)}{V_p} \tag{26}$$

where V_p is the total effective pore volume of the macroscopic porous medium. At this point, the theoretical upgrade from microscopic pore interface dynamics to macroscopic porous media network imbibition characteristics is complete.

To implement the dynamic simulation of the aforementioned multiscale fractal model, a customized numerical solver was developed using the MATLAB platform. The core logic of the algorithm is described below. First, the fluid physical properties and the fractal geometric parameters of the porous medium are initialized. Subsequently, the solver system is called at the microscopic scale to calculate the transient imbibition dynamics of the single-capillary interface, during which analytical or numerical methods are adaptively selected based on actual working conditions. Finally, discretized numerical integration is performed over the global pore size interval using Eqs. (25) and (26) to output the dynamic evolution of the total macroscopic imbibition flow rate and cumulative volume. The complete computational architecture and logic flow are shown in Fig. 3**.**

3. Model validation

3.1. *Verification of the explicit analytical solution*

A benchmark simulation is conducted using a vertical capillary with a radius of 100 μm to systematically evaluate the accuracy and stability of the three aforementioned solution strategies (Lambert W analytical solution, implicit iteration, and explicit Euler method). To facilitate the clear capture of transient percolation characteristics in micropores, the high-viscosity model fluid shown in Table 1 was uniformly used for single-tube mechanism analysis. Furthermore, capillary-driven imbibition theoretically requires an infinite duration to reach complete equilibrium, and the imbibition rate significantly approaches zero during the later stages of the actual physical process. Consequently, 95% of the theoretical equilibrium distance is defined as the effective equilibrium point (as shown in Fig. 4**a**).

Fig. 4 illustrates the dynamic evolution of spontaneous capillary imbibition under various solution schemes. The results show that the Lambert W explicit analytical solution and the implicit bisection iterative solution overlap almost perfectly across the entire time domain. This consistency cross-validates the accuracy of the proposed physical model and the explicit analytical solution. In contrast, the computational precision of the explicit Euler integration is highly dependent on the time step Δt. As depicted in the local magnifications of Figs. 4**(b)** and 4**(d)**, the truncation error of the Euler scheme leads to a significant overestimation of the interface advancement distance when a large time step is employed. The numerical solution gradually converges to the theoretical benchmark only when Δt is reduced to 0.001 s. In summary, traditional explicit numerical schemes are plagued by substantial truncation errors and inherent instabilities when resolving the high-speed nonlinear dynamics of early-stage imbibition. In contrast, the Lambert W analytical solution achieves high precision while maintaining an explicit form, effectively avoiding the iterative burden in computation. Consequently, the Lambert W analytical solution is adopted for all following large-scale parameter sweeps and cross-scale simulations.

3.2. *Validation at the microscopic scale*

To verify the validity of the new model, we compared its results with three classical models (Fig. 5). Except for the parameters explicitly noted in the figure, all other settings are identical to those in Section 3.1. Among them, the Washburn model [13] neglects gravitational effects, leading to an unphysical and unbounded increase in the predicted imbibition distance over time. By incorporating gravity, the model by Cai et al. [16] successfully predicts an equilibrium imbibition limit of 0.0734 m. Furthermore, compared to Cai et al., the model by Wang et al. [32] shares the identical equilibrium limit but accounts for the dynamic contact angle. This creates additional viscous resistance early on, extending the time to reach 95% equilibrium from 1245 s to 1847.4 s. Finally, comparing the proposed model with that of Wang et al. reveals that surface roughness fundamentally alters both the thermodynamic and kinetic behaviors of the system. The attenuated capillary driving

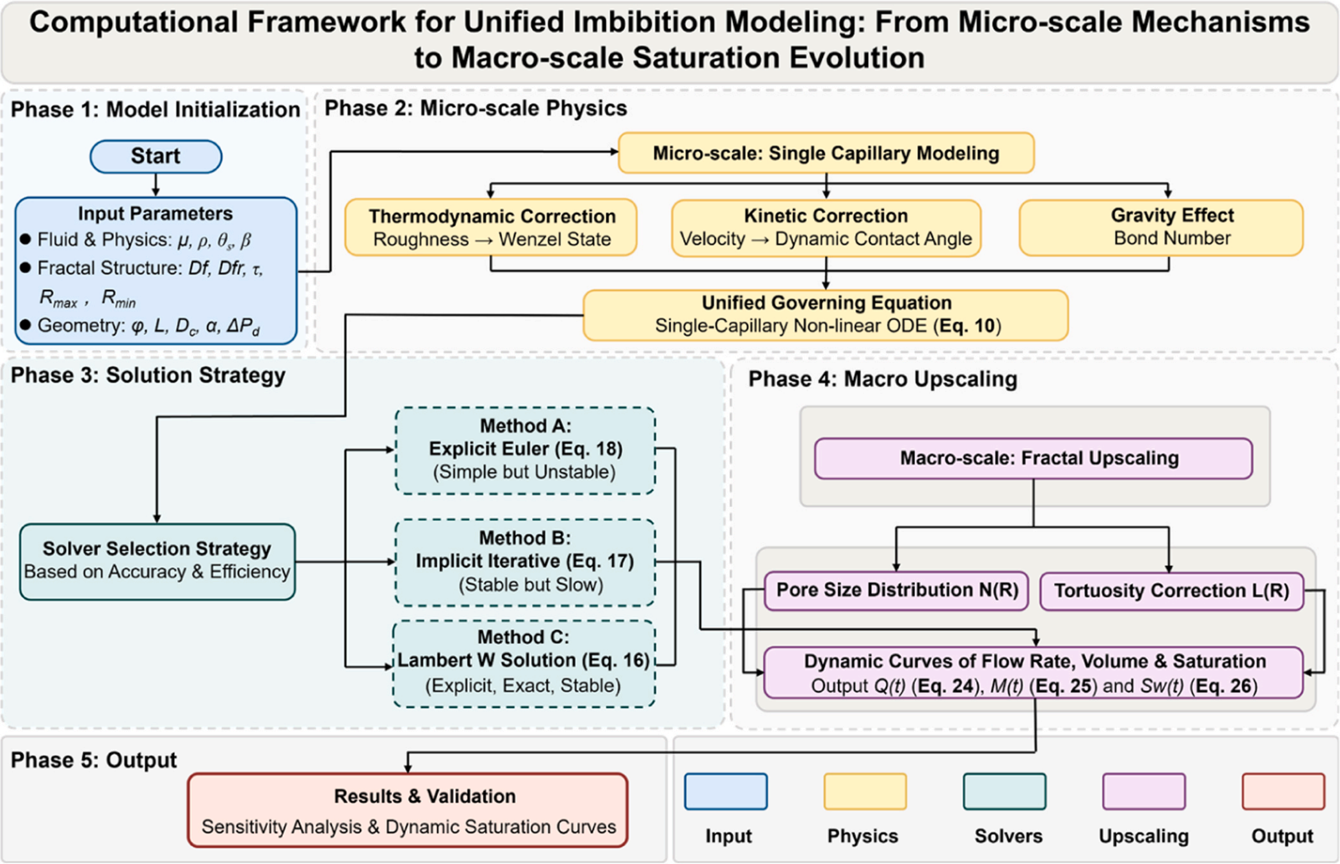

Fig. 3. Numerical solution logic and core computational framework for the multiscale unified imbibition model.

Table 1
Input parameters for the microscopic simulation of imbibition dynamics in a single capillary.

Parameter	Symbol	Value	Unit
Liquid viscosity	μ	0.1	Pa·s
Liquid density	ρ	1000	kg/m^3
Surface tension	σ	0.072	N/m
Static contact angle	θ_S	60	°
Dynamic contact angle coefficient	β	1	—
Maximum length scale for fractal scaling	Λ	1×10^{-4}	m
Edge length of equivalent roughness element	l	1×10^{-6}	m
Surface roughness fractal dimension	D_{fr}	2.5	—
Capillary inclination angle	α	90	°

force drastically reduces the final equilibrium distance to 0.0232 m. It is shown that ignoring the dynamic contact angle leads to an over-estimated initial imbibition rate, while neglecting surface roughness results in an exaggerated final imbibition capacity. Ultimately, the new model resolves prior shortcomings, offering a more rigorous and physically consistent framework for spontaneous imbibition.

3.3. Validation at the macroscopic scale

To verify the applicability of the proposed model, predicted results are compared with experimental data for two real porous materials. The simulation parameters, including geometric and fluid properties, are provided in Table 2. The proposed fractal model predictions are compared with experimental data [54,55] in Fig. 6. The model predictions match closely with experimental data across different scales, from mesoporous silica with nanoscale pores (Fig. 6**a**) to Bentheim sandstone with micron-scale pores (Fig. 6**b**). Nearly all data points lie within a ±5% deviation band.

Furthermore, the coefficient of determination (R^2) and root-mean-square error ($RMSE$) were employed for statistical evaluation. $R^2 = 0.9994$ ($RMSE = 0.0004$ g) for Huber et al., and $R^2 = 0.9966$ ($RMSE = 0.0427$ g) for Olafuyi et al. Overall, the model predictions consistently follow the experimental trends across distinct pore structures with minimal absolute errors. These statistical metrics demonstrate the high accuracy and reliability of the proposed model in capturing the imbibition dynamics of porous media.

4. Results and discussion

4.1. Computational performance and numerical stability

Although Section 3.1 has qualitatively demonstrated the accuracy advantages of the Lambert W analytical solution, a rigorous quantitative evaluation of the algorithmic characteristics of the three proposed methods is further required. Specifically, evaluating their computational cost, numerical stability boundaries, and convergence behavior provides comprehensive justification for selecting the Lambert W method for subsequent macroscopic upscaling, ultimately balancing accuracy and iterative efficiency. This section uses the Lambert W analytical solution [56] as a benchmark to systematically evaluate the numerical performance of the implicit iterative method and the explicit Euler method (Fig. 7). Specifically, Figs. 7**(a)** and 7**(b)** demonstrate the superior stability of the implicit algorithm. Throughout the simulation, the global residual of the implicit solution decays steadily from 10^{-13} to 10^{-16}, effectively eliminating the risk of numerical divergence caused by error accumulation. Furthermore, although the enhanced nonlinearity in the late imbibition stage leads to a slight increase in iterations per step (stabilizing at 40–50), the convergence flag remains consistently at 1

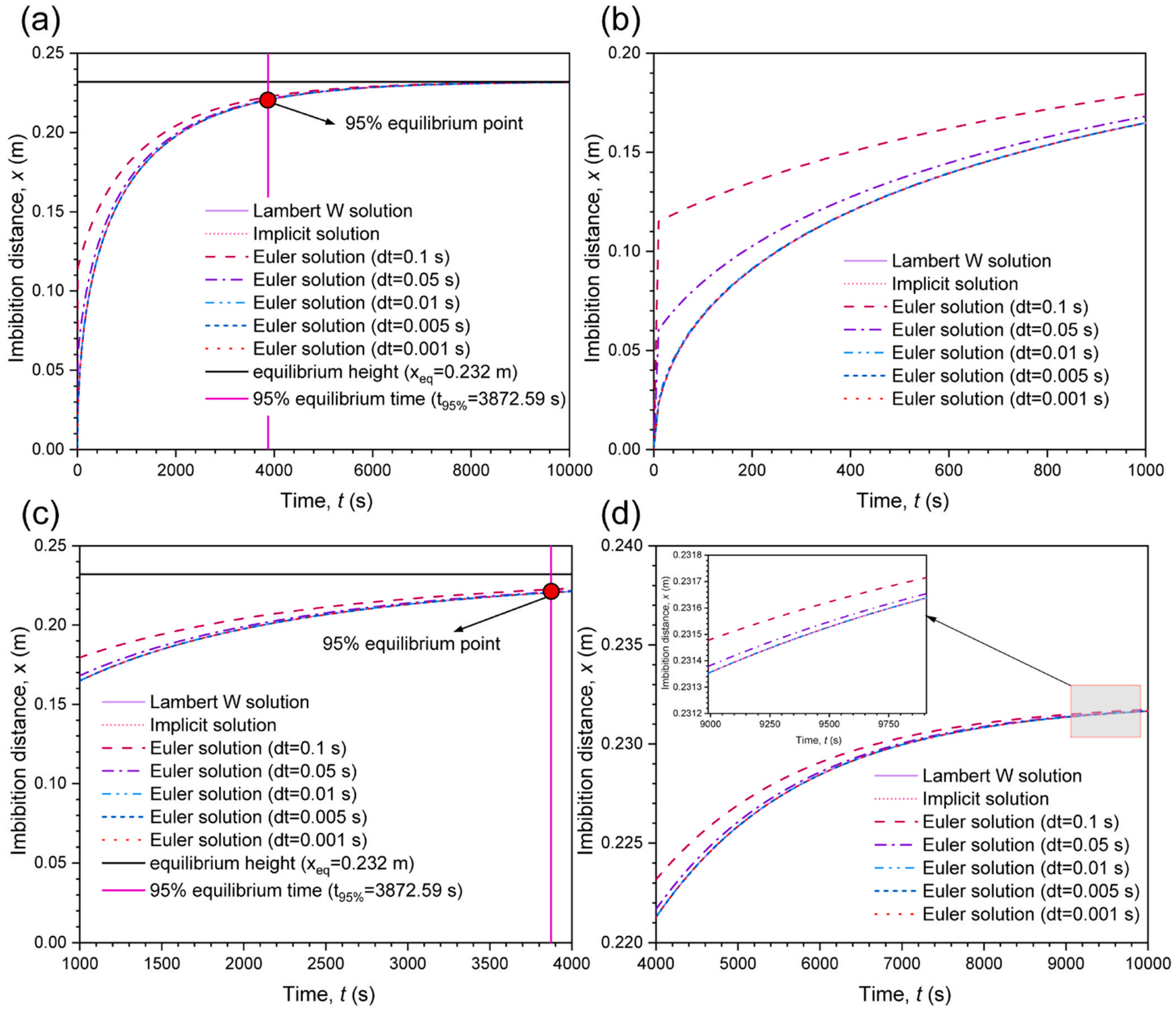

Fig. 4. Evolution of imbibition distance over time in a single vertical capillary using three different solution methods. (a) Overall evolution process; (b) Close-up of the initial rapid phase (0 s $\leq$ t $<$ 1000 s); (c) Intermediate equilibrium phase (1000 s $<$ t $\leq$ 3872.59 s); (d) Final equilibrium phase (t $>$ 3872.59 s).

over the entire time domain. This demonstrates the robust stability of the algorithm in handling strongly nonlinear capillary flows.

In terms of computational accuracy, the explicit Euler method is highly sensitive to the choice of time step Δt. As illustrated in Fig. 7**(d)**, the truncation error of the Euler solution is significantly reduced only when Δt is decreased from 0.1 s to 0.001 s. Meanwhile, as the capillary driving force gradually diminishes, the errors across all time steps converge as the imbibition progresses. Fig. 7**(e)** presents the error vs. time step relationship on a log-log scale. The results show that the reduction slopes for both maximum and average errors consistently follow the theoretical benchmark, verifying the first-order convergence characteristics of the explicit scheme.

Beyond accuracy, computational cost is a crucial metric for evaluating algorithmic utility. Fig. 7**(c)** compares the total computational time required by different solving strategies. The results indicate that while the explicit Euler method is conceptually straightforward, achieving acceptable accuracy (Δt = 0.001 s) results in a total time of 0.277 s. This duration is more than 90 times that of the implicit solver (0.003 s) at the same precision level. Although the Lambert W analytical solution involves a slightly higher computational cost (0.010 s) due to transcendental function evaluations, it provides explicit analytical solution in a concise algebraic form. This approach effectively eliminates the truncation errors and step size sensitivity inherent in discrete numerical schemes. Consequently, the Lambert W solution is consistently adopted for all subsequent mechanism analyses and macroscopic upscaling.

4.2. Control mechanisms of the apparent dynamic contact angle at the pore scale

In contrast to conventional models assuming a constant contact angle, actual dynamic wetting results from the intense coupling of diverse physical processes. This section systematically examines how three core factors independently affect the dynamic contact angle: the scale effect of pore size, the static inhibition mechanism from surface roughness, and the nonlinear drag effect caused by dynamic imbibition velocity.

4.2.1. Scale effects of pore size

To more clearly capture and visualize the transient evolution of the

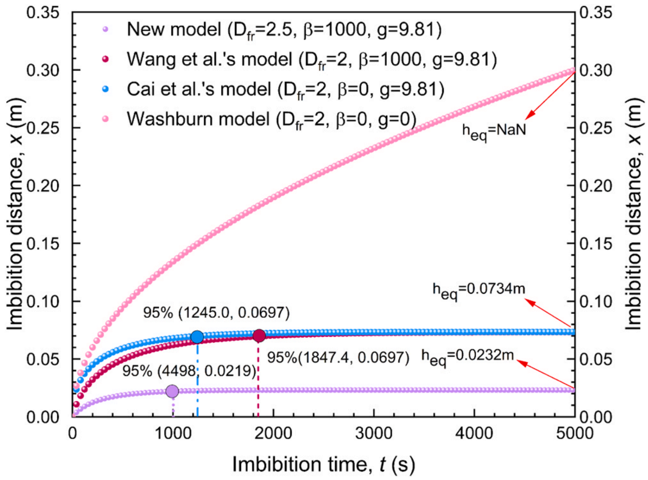

Fig. 5. Comparison of the dynamic evolution of spontaneous capillary imbibition under various physical mechanisms. (Solid symbols denote the time and corresponding coordinates for each curve to reach 95% of the theoretical equilibrium distance.).

Table 2

Geometric parameters of porous media and fluid physical properties used in the model validation.

Parameter	Symbol	Unit	Fig. 6 **(a):** Mesoporous silica	Fig. 6 **(b):** Berea sandstone
Fluid properties				
Fluid viscosity	μ	Pa·s	0.95×10^{-3}	1×10^{-3}
Fluid density	ρ	kg/m^3	1000	1000
Interfacial tension	σ	N/m	0.07225	0.0727
Static contact angle	θ_s	°	0	0
Geometric parameters				
Dynamic contact angle coefficient	β	—	1000	100
Effective length	L	cm	2.56	2.56
Effective diameter	D_C	cm	0.465	2.5
Porosity	φ	—	0.30	0.23
Inclination angle	α	°	90	90
Fractal structure				
Pore size fractal dimension	D_f	—	1.83	1.93
Surface roughness fractal dimension	D_{fr}	—	2.66	2.19
Tortuosity	τ	—	2.17	2.73
Minimum pore radius	$R_{\min}$	μm	0.0001	0.1
Maximum pore radius	$R_{\max}$	μm	0.0254	25
Edge length of equivalent roughness element	l	m	1×10^{-6}	1×10^{-6}
Maximum length scale for fractal scaling	Λ	m	1×10^{-4}	1×10^{-4}
Numerical settings				
Total simulation time	t_{end}	s	5000	50
Number of time steps	n_t	—	2000	2000
Number of pore radius discretizations	n_R	—	5000	3000

dynamic contact angle within micropores, the fluid viscosity is appropriately increased to 1 Pa·s in the simulations. Fig. 8**(a)** illustrates the temporal evolution of the imbibition velocity under various micro-pore sizes where R ranges from 100 nm to 1000 μm. The results indicate that the transient advancement of the fluid is governed by the competition between viscous resistance and gravity. Pore size exerts a significant controlling effect on the imbibition velocity, exhibiting a distinct nonlinear scale effect. For micropores ($R \leq 1$ μm), the flow is primarily dominated by viscous friction, which is consistent with the classical Washburn regime [13,57]. Consequently, the velocity undergoes a sharp decay during the initial stage before transitioning into a slow and steady advancement. As pore size increases, the hydraulic conductivity is significantly enhanced. For large pores such as $R = 1000$ μm, the fluid exhibits relatively high initial mobility. However, the weak capillary driving force causes the liquid column to reach equilibrium with gravity within approximately 200 s. Simultaneously, the flow velocity drops sharply and quickly returns to zero.

Fig. 8**(b)** reveals the dynamic evolution of the apparent dynamic contact angle during imbibition and its sensitivity to pore size. Although all cases converge to the prescribed static intrinsic value of 60° at the end of imbibition, their transient evolution exhibits significant non-monotonic characteristics. Specifically, nanoscale micropores severely restrict the flow velocity due to immense viscous drag, resulting in a marginal dynamic increase in the contact angle. According to classical dynamic wetting theories [31,58], a high flow velocity significantly increases the dynamic contact angle. Our millimeter scale simulations clearly show this effect, as a very high initial velocity causes the contact angle to rise sharply. However, this angle quickly decreases as the fluid reaches equilibrium with gravity. In contrast, intermediate pores reside in a physical balance zone between viscous and gravitational forces. These pores can maintain a high flow velocity for a prolonged duration, thereby exhibiting the most pronounced dynamic contact angle variation. These findings demonstrate that actual dynamic wettability does not vary monotonically with pore size. To prevent severe misinterpretations of multiscale imbibition dynamics caused by assuming a constant static contact angle, numerical simulations must incorporate dynamic corrections based on the local velocity field [59].

4.2.2. *Static inhibition mechanism induced by surface roughness*

This section deeply investigates the evolution of imbibition dynamics under the coupled influence of capillary radius R and wall roughness fractal dimension D_{fr} (Fig. 9). Figs. 9**(a)** and 9**(b)** clearly demonstrate the significant attenuating effect of roughness on imbibition performance. As D_{fr} increases from 2.0 (smooth) to 2.8 (highly rough), the 95% equilibrium imbibition distance (denoted as $x_{95\%}$) exhibits a sharp monotonic decreasing trend. This phenomenon indicates that the presence of roughness induces a prominent static inhibition mechanism. Specifically, the contact line pinning effect caused by rough microelements increases the effective apparent contact angle [60]. This increase substantially reduces the capillary driving pressure difference and lowers the theoretical imbibition equilibrium point. Furthermore, Fig. 9 **(c)** clearly delineates a capillary inhibition zone based on the fractal scaling law. Under high roughness conditions (such as $D_{fr} = 2.8$), the imbibition velocity rapidly drops to zero at a relatively low imbibition distance. This observation confirms that once the roughness exceeds a specific threshold, the mass transfer capacity of the micropores becomes severely impaired. This finding aligns with the theories of Shen et al. [26] and Yang et al. [28] regarding flow resistance in rough networks, even though they employed different methods to characterize wall roughness. Consequently, these pores transform into ineffective flow channels.

The contour plots in Figs. 9**(d)** to 9**(f)** further reveal the coupled effects of R and D_{fr}. Fig. 9**(d)** illustrates a diagonal distribution for the $x_{95\%}$, indicating that the region with small pore size and high roughness experiences the most severe imbibition inhibition. This scale sensitivity stems from the superposition of three physical mechanisms. First, rough microelements occupy a larger relative geometric proportion in micropores. Second, the capillary driving force is more easily weakened by rough structures in smaller pores. Third, the inherently high viscous resistance in small pores further amplifies the additional drag induced by roughness. This extreme sensitivity of viscous dissipation to surface asperities under tight confinement has been rigorously confirmed by recent hydrodynamic investigations [61,62]. Fig. 9**(e)** shows that under a constant pore size, both the equilibrium time and distance decrease as

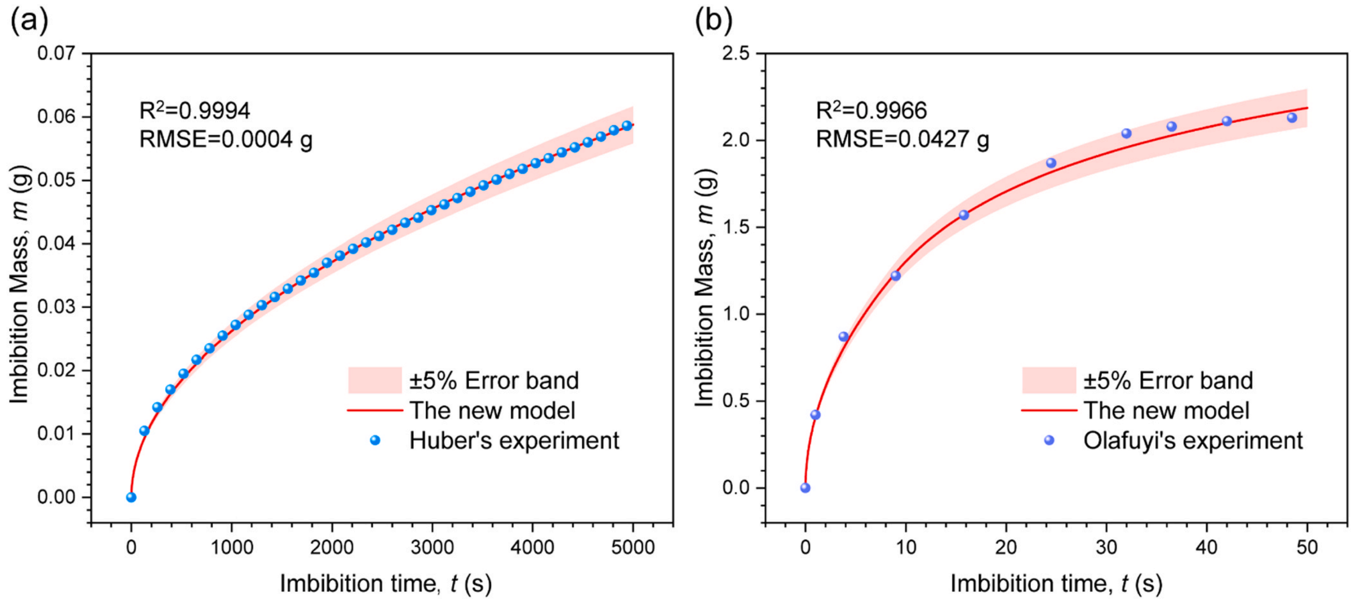

Fig. 6. Comparison between model predictions and experimental data. (a) Imbibed mass in nanoscale mesoporous silica [54]; (b) Imbibed mass in micron-scale Bentheim sandstone [55].

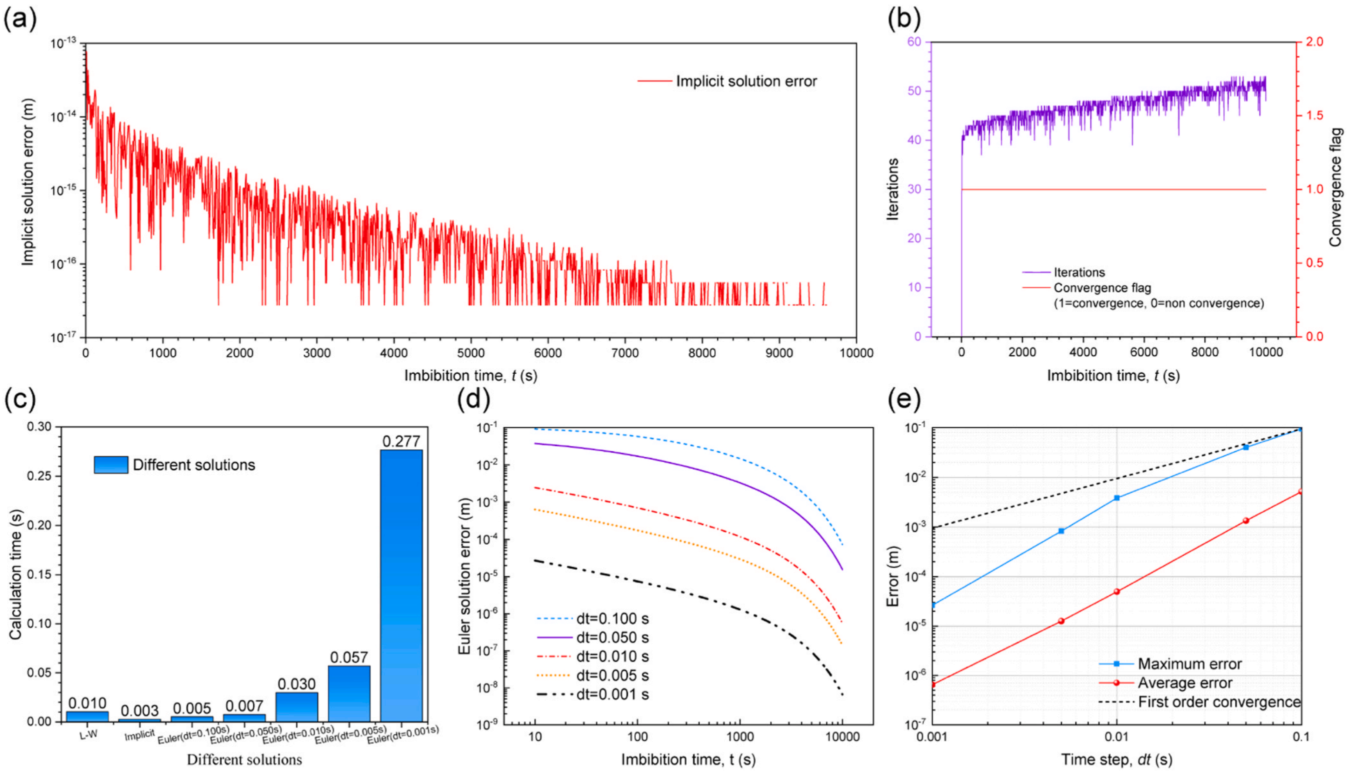

Fig. 7. Numerical stability and error analysis of different solving methods. (a) Error of the implicit solution; (b) convergence of the implicit solver; (c) computational efficiency comparison; (d) error of the explicit Euler method; (e) convergence of the explicit Euler method.

the wall roughness increases. Fig. 9**(f)** indicates that the flow velocity peaks in regions characterized by large pores and low roughness. Conversely, high roughness drastically reduces the velocity and forces it to approach zero in small pores. In summary, wall roughness directly impairs the capillary driving force and severely retards the initial imbibition acceleration. This inhibitory effect becomes particularly pronounced in small pores and ultimately degrades the fluid transport capacity of micropores.

4.2.3. Nonlinear retardation mechanism of the dynamic contact angle

Recent fractal models [63,64] have shown that neglecting dynamic wettability leads to a severe overestimation of imbibition rates. However, the underlying micro-scale mechanisms remain unclear. Therefore, this section examines the coupled influence of the dynamic contact angle coefficient β and capillary radius R on imbibition dynamics (Fig. 10). Figs. 10**(a)** and 10**(b)** demonstrate that β functions purely as a kinetic dissipation term. According to fundamental wetting dynamics [31], this

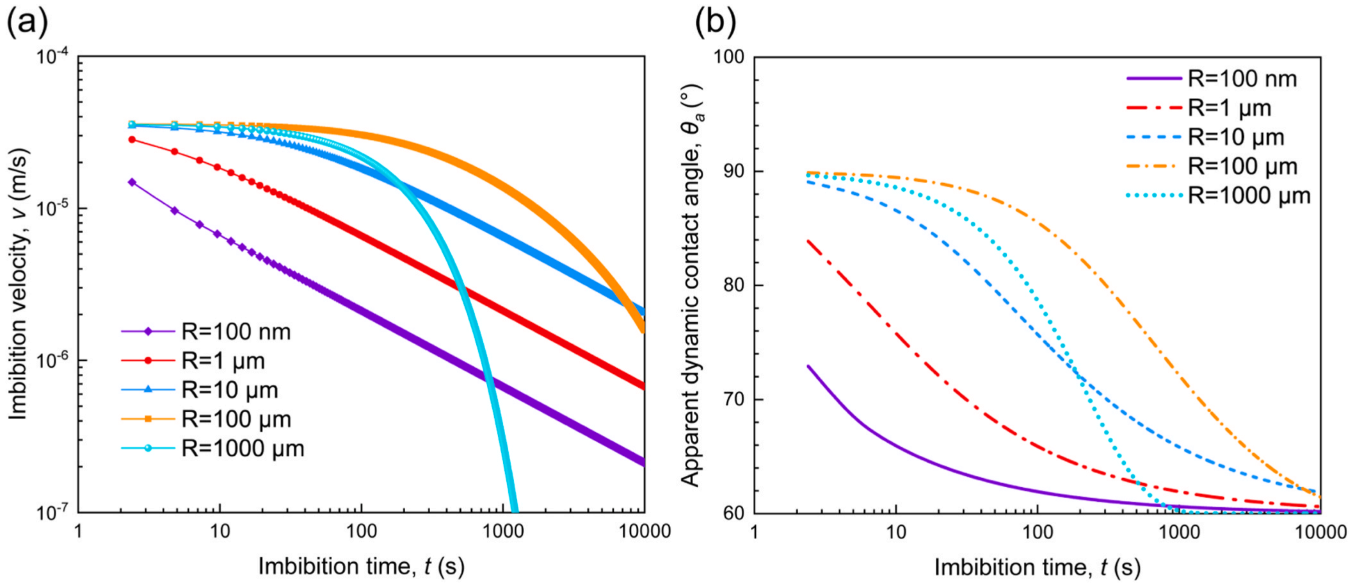

Fig. 8. Effect of capillary radius on the apparent dynamic contact angle. (a) Temporal evolution of imbibition velocity. (b) Variation of the apparent dynamic contact angle with imbibition time. (Fixed simulation parameters: $\mu = 1$ Pa·s, $\theta_s = 60°$, $\beta = 1000$ and $D_{fr} = 2$. Other fluid properties and geometric parameters are detailed in Table 1.).

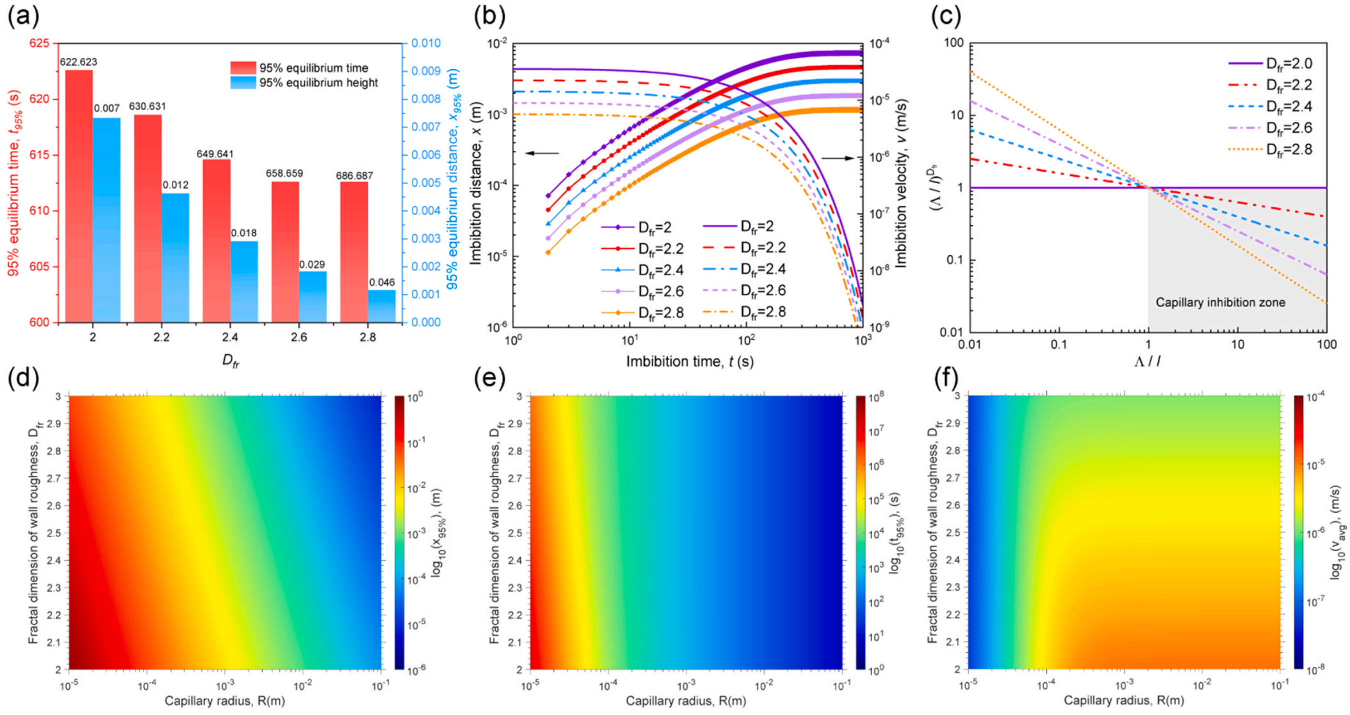

Fig. 9. Comprehensive analysis of the combined effects of the roughness fractal dimension D_{fr} and capillary radius R on imbibition performance. (a) Variations of the 95% equilibrium time $t_{95\%}$ and 95% equilibrium imbibition distance $x_{95\%}$ with D_{fr}. (b) Temporal evolution of imbibition distance and velocity under different values of D_{fr}. (c) Analysis of the capillary inhibition effect induced by wall roughness. The contour plots in (d), (e), and (f) illustrate the influence of R and D_{fr} on $x_{95\%}$, $t_{95\%}$, the average velocity v_{avg} respectively. (Fixed simulation parameters are $\mu = 1$ Pa·s, $\theta_s = 60°$, $\beta = 1000$. Other fluid properties and geometric parameters are detailed in Table 1.).

effect purely represents energy dissipation at the moving contact line. Thus, it does not alter the thermodynamic equilibrium point, ensuring the final imbibition distance remains strictly constant. However, the transient evolutionary path towards equilibrium is highly sensitive to β. When β exceeds a critical threshold, the required imbibition time grows exponentially, accompanied by pronounced velocity retardation. Fig. 10 **(c)** identifies the root cause of this retardation effect. The apparent contact angle remains insensitive to β at low velocities. Conversely, at high flow velocities such as $v = 0.1$ m/s, the angle surges nonlinearly with increasing β, rapidly surpassing 90° and reaching up to 140°.

The contour plots in Figs. 10**(d)** to 10**(f)** further elucidate the interaction mechanism between pore size and β. The results indicate that the retardation effect of the dynamic contact angle is significantly more pronounced in large pores. In nanoscale micropores, inherently high

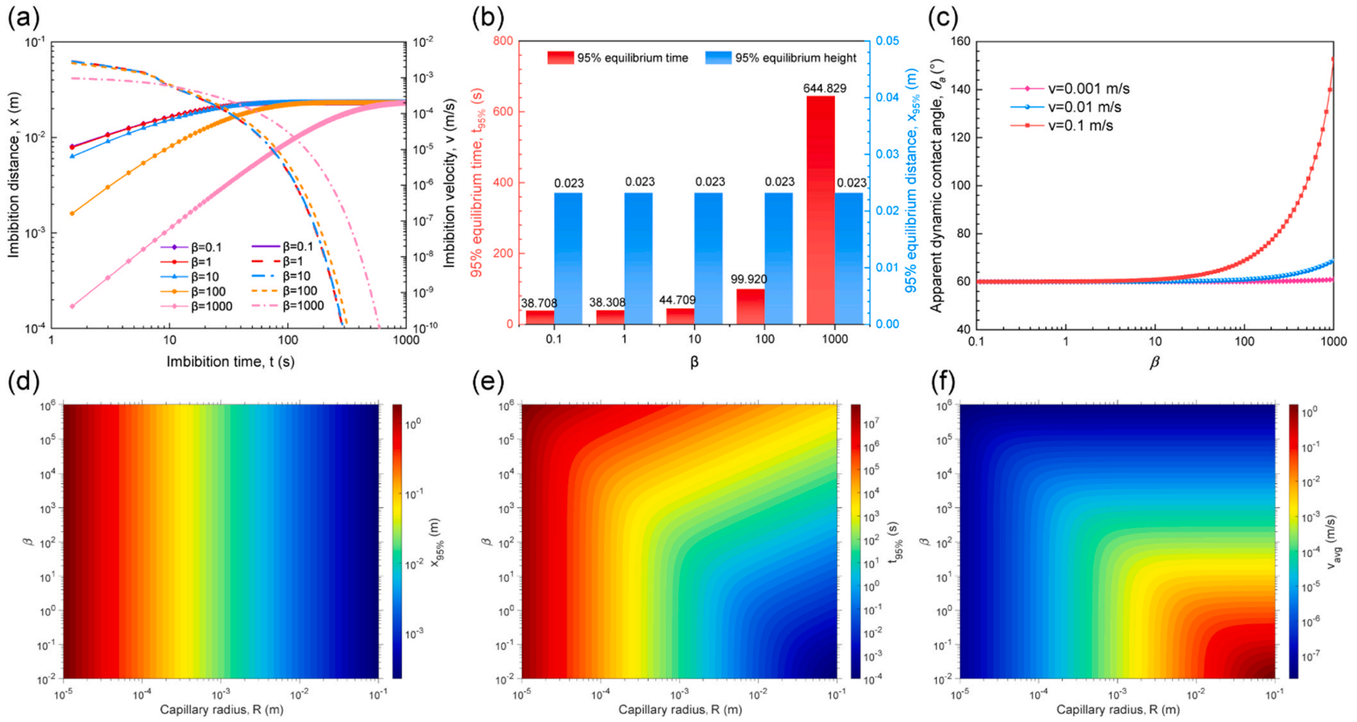

Fig. 10. Comprehensive analysis of the combined effects of the dynamic contact angle coefficient β and capillary radius R on imbibition performance. (a) Temporal evolution of imbibition distance and velocity under different values of β. (b) Variations of the 95% equilibrium time $t_{95\%}$ and equilibrium imbibition distance $x_{95\%}$ with β. (c) Variations of the apparent dynamic contact angle with β under different imbibition velocities. (d) to (f) Contour plots illustrating the influence of R and β on (d) $x_{95\%}$, (e) $t_{95\%}$, and (f) v_{avg}. (Fixed simulation parameters are $\mu = 1$ Pa·s, $\theta_s = 60^\circ$, and $D_{fr} = 2$. Other fluid properties and geometric parameters are detailed in Table 1.).

viscous drag naturally restricts flow velocity and prevents the activation of the dynamic contact angle effect. Conversely, the extremely high initial velocity potential in large pores instantaneously triggers a dramatic surge in the dynamic contact angle. Furthermore, although large channels possess tremendous permeability potential, a marginal increase in β induces a substantial velocity decay. Consequently, neglecting dynamic wettability corrections for large channels in multiphase flow simulations of macroscopic porous media will result in a severe overestimation of early imbibition mass transfer efficiency.

4.3. Competitive mechanisms between gravity and capillary forces

While existing models incorporate inclination angles to account for gravity [17], their quantitative effects at the microscopic pore scale remain unexplored. To address this gap, Fig. 11 illustrates the influence of inclination angle α on spontaneous imbibition across various pore scales. During upward imbibition, the gravitational component serves as the primary resistance and exhibits a pronounced scale dependence. Fig. 11**(a)** shows that for large pores where $R = 100$ μm, the imbibition curves are highly sensitive to the α. Both the imbibition distance and velocity drop sharply as the angle increases. Conversely, Figs. 11**(b)** and 11**(c)** demonstrate that curves for different α tend to converge as the pore size decreases. The curves stay close together because the strong capillary force is much larger at the start and hides the effect of gravity [65]. Small differences only appear later when the liquid column is high enough to balance the capillary pressure. Eq. (14) indicates that the equilibrium distance is inversely proportional to the sine of the α. During the initial stage, gravitational resistance remains negligible. Since the dynamics are primarily governed by capillary pressure, the initial velocities remain nearly identical regardless of the angle. However, gravitational resistance accumulates rapidly as the liquid column grows within the capillary. Larger α lead to a faster increase in resistance, which results in more drastic velocity decay. Finally, when the velocity reaches zero, the constant capillary driving force is perfectly balanced by the hydrostatic head generated by gravity.

4.4. Dimensionless scaling and mechanical similarity of a single capillary

To reveal the competition and dominance mechanisms of coupled physical mechanisms during different imbibition stages, the single capillary governing equation (Eq. 10) is transformed into a dimensionless form. The full derivation is provided in the **Appendix**. The pore radius R is selected as the characteristic length while $t_c = 4\mu R/(\sigma\cos\theta_s)$ is used as the characteristic time. The resulting dimensionless velocity equation is governed by three core dimensionless parameters as follows.

$$v^* = \frac{dx^*}{dt^*} = \frac{r - Box^*}{x^* + \beta/4} \tag{26}$$

where $x^* = x/R$ is the dimensionless imbibition displacement. The term$r = \frac{A_R}{A_s} = \left(\frac{l}{\lambda}\right)^{2-D_{fr}}$ is the wall roughness factor. The parameter β is the dynamic contact angle coefficient. The Bond number $Bo = \rho g R^2/2\sigma\cos\theta_s$ is the ratio of gravity to capillary forces.

Fig. 12 illustrates the analysis of dimensionless imbibition dynamics and mechanical mechanisms. The entire imbibition process is not governed by a single force across time scales. The first phase is the early capillary dominant stage, which is primarily controlled by the roughness fractal dimension D_{fr} because the liquid column remains extremely short while viscous and gravitational resistance are negligible. As schematically illustrated in Figs. 12**(a)** and 12**(d)**, the upward capillary driving force (red arrow) dominates this early stage. Meanwhile, the downward viscous and gravitational resistances (blue and black arrows) are minimal. When D_{fr} increases, the wall pinning effect directly weakens the effective capillary force. This reduction is visually represented by the shrinking red arrows in Fig. 12**(d)**. As a result, both the dimensionless

(a) Large Pores: R = 100 μm

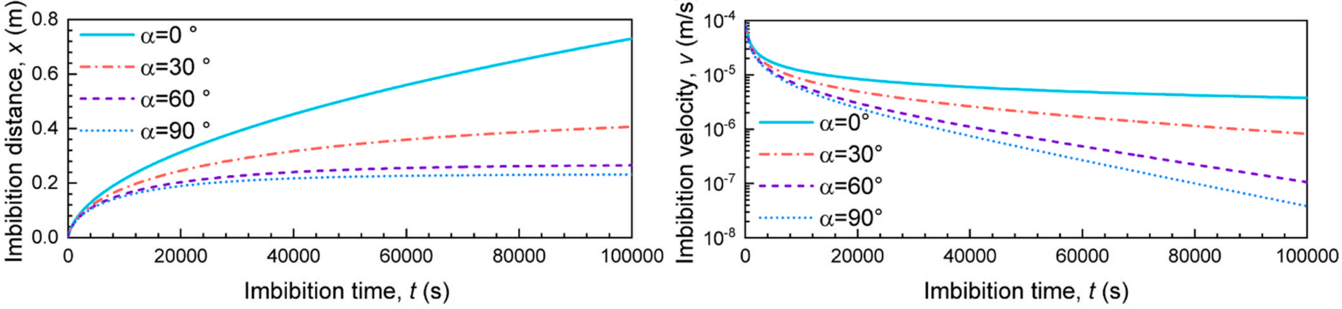

(b) Micro Pores: R = 10 μm

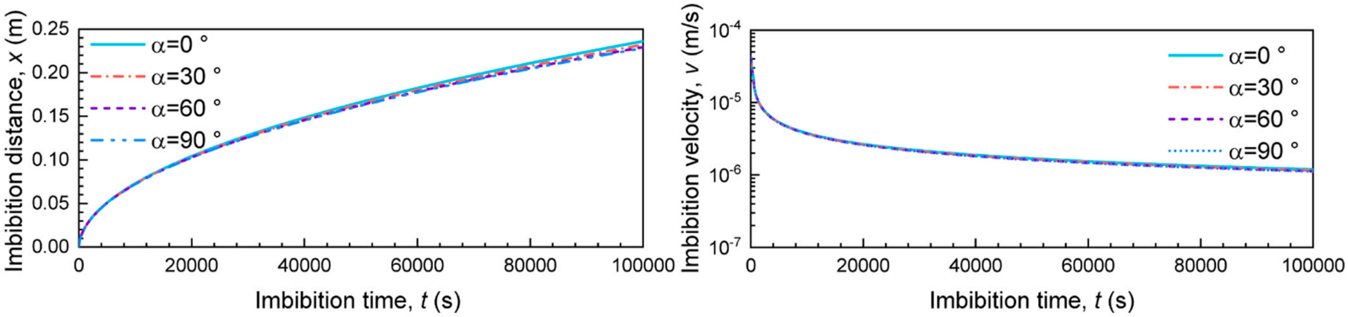

(c) Nano Pores: R = 1 μm

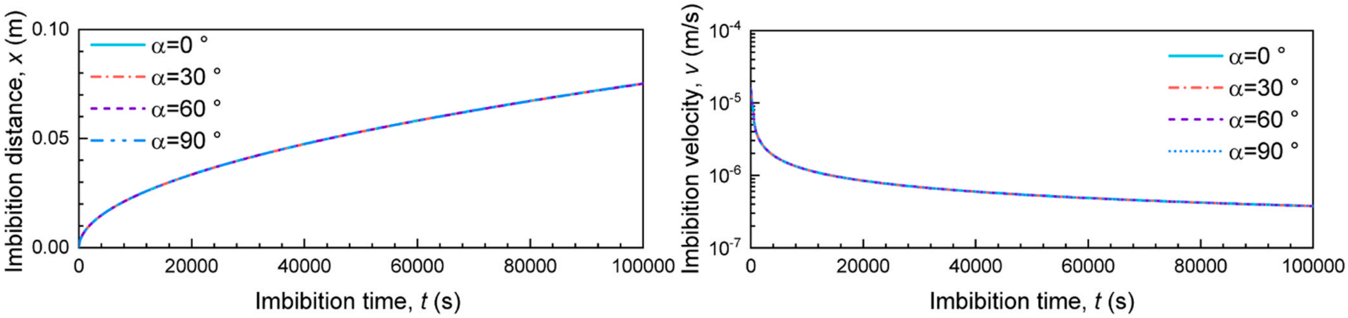

Fig. 11. Influence of inclination angle α on spontaneous imbibition at different pore scales. (a) $R = 100$ μm ; (b) $R = 10$ μm ; (c) $R = 1$ μm. (In each plot, the left and right sides show imbibition distance and velocity, respectively. Fixed simulation parameters are $\mu = 1$ Pa·s, $\theta_s = 60^\circ$, $\beta = 1000$ and $D_{fr} = 2.5$. Other fluid properties and geometric parameters are detailed in Table 1.).

imbibition distance and initial velocity are significantly suppressed.

The second phase is the middle viscous dominant stage, where fluid viscous dissipation grows linearly to compete with the capillary force as the interface advances. Figs. 12**(b)** and 12**(e)** indicate that the dynamics shift to be dominated by β. As physically illustrated in Fig. 12**(e)**, the downward viscous resistance (blue arrow) grows significantly to compete with the capillary force. A larger β drastically amplifies this transient viscous resistance at the interface. This amplification is visually depicted by the lengthening blue arrows, which ultimately inhibit the advancement rate.

Finally, the process enters the late gravity viscous coupled stage as the hydrostatic head continues to accumulate while the liquid column progresses further into the capillary. Figs. 12**(c)** and 12**(f)** reveal the decisive role of the Bond number *Bo* on the ultimate state of imbibition. As depicted in Fig. 12**(f)**, the downward gravitational resistance (black arrow) accumulates progressively with the rising liquid column. A larger *Bo* indicates that gravity dominates the system much earlier. This early dominance is represented by the rapidly lengthening black arrows. Consequently, the net driving force is depleted prematurely, forcing the system to reach equilibrium at a lower height.

Fig. 13 presents the evolution of dimensionless imbibition characteristics ($t^*_{95\%}$, $x^*_{95\%}$, v^*_{avg}) within the parameter space of the roughness fractal dimension D_{fr}, apparent dynamic contact angle β, and Bond number *Bo*. As shown in Fig. 13**(a)**, the dynamic response of the system exhibits strong nonlinearity and parameter heterogeneity. The extreme values of these characteristics do not transition smoothly but are strictly confined to specific corners of the parameter space. For example, the maximum equilibrium distance occurs in the region with low *Bo*, low D_{fr}, and low β. The longest equilibrium time is found in the region with low *Bo*, high D_{fr}, high β. Notably, the maximum average velocity is concentrated in the area with high *Bo*, low D_{fr}, and low β. This phenomenon occurs because a large *Bo* forces the fluid to stop after an extremely short climbing distance. The almost instantaneous completion of the process inevitably leads to the highest calculated average velocity.

Figs. 13**(b)** and 13**(c)** present the evolution of dimensionless imbibition characteristics within a two dimensional parameter space. For $x^*_{95\%}$, the contour lines exhibit strict vertical stratification under both capillary dominant ($Bo = 0.01$) and gravity dominant ($Bo = 100$) conditions. This pattern indicates that $x^*_{95\%}$ depends primarily on D_{fr} and is entirely independent of β. Specifically, a lower D_{fr} is favorable for achieving a higher equilibrium imbibition distance. Conversely, the equilibrium time $t^*_{95\%}$ is primarily controlled by β and shows a monotonic upward trend as it increases. However, the average velocity v^*_{avg}

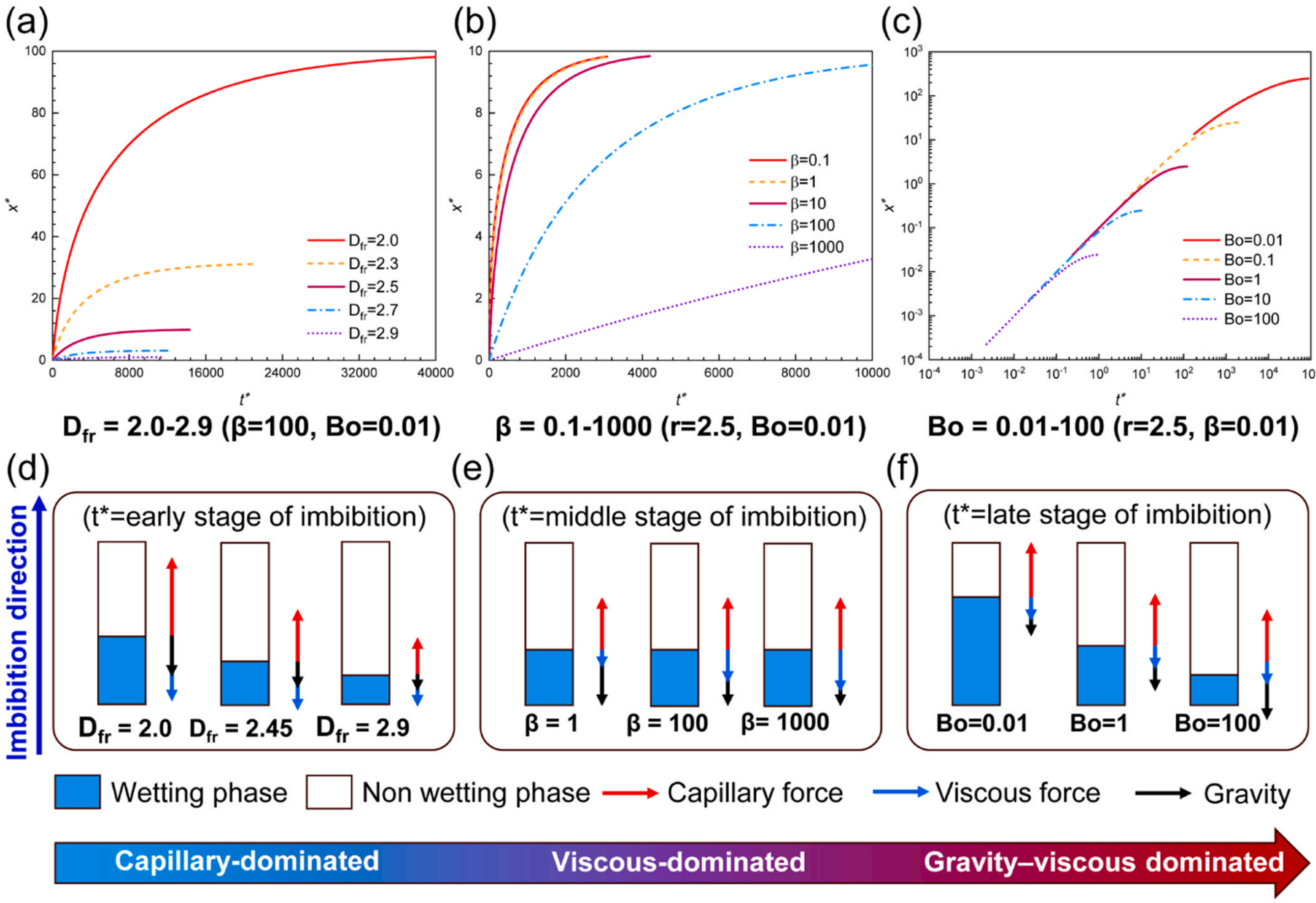

Fig. 12. Analysis of dimensionless imbibition dynamics and force balance mechanisms. The effects of (a) the roughness fractal dimension D_{fr}, (b) the dynamic contact angle coefficient β, and (c) the Bond number Bo on the evolution of the dimensionless imbibition distance x^* with the dimensionless time t^* are presented. The schematic diagrams of force balance in (d), (e), and (f) reveal the dominant mechanisms across different imbibition stages under the corresponding parameters.

exhibits a dual dependence and reaches its peak only when both D_{fr} and β are at their minimums. By comparison, under the gravity dominant mechanism where $Bo = 100$, the high velocity region of v^*_{avg} is significantly suppressed and restricted to a much narrower range of low D_{fr} and low β. These results reveal that the gravitational effect substantially weakens the flow velocity, allowing high speed flow to be maintained only under extreme conditions with the smoothest walls and the most stable contact angles.

4.5. Fractal imbibition dynamics in macroscopic porous media

This section expands the research perspective from a single capillary to a macroscopic porous medium. Based on the established fractal model, we systematically evaluate the sensitivity of macroscopic imbibition dynamics to microscopic parameters under the influence of multiple competing forces.

4.5.1. Effect of the apparent dynamic contact angle on imbibition

Fig. 14 illustrates the synergistic effects of the β and D_{fr} on macroscopic spontaneous imbibition characteristics. Figs. 14**(a)** and 14**(d)** reflect the threshold effect and time lag caused by the dynamic contact angle. The imbibition process remains in a dynamically insensitive region with a constant $t_{95\%}$ when $\beta < 10$. Once $\beta > 10$, the system enters a dynamically sensitive region where $t_{95\%}$increases exponentially. This mechanism is further confirmed by a significant rightward shift of the saturation curves in Fig. 14**(a)**. A high value such as $\beta = 1000$ substantially weakens the effective capillary driving force and thus causes a severe time lag.

Furthermore, Figs. 14**(a)** and 14**(b)** indicate that the suppression effect of β is primarily concentrated in the early stage of imbibition. As the flow velocity naturally decays, the dynamic effect gradually weakens, causing the rate and saturation curves under different β values to converge in the late stage. Notably, unlike the mechanism of β, D_{fr} directly suppresses the effective wettability of the system. As illustrated in Fig. 14**(c)**, the final imbibition volume decreases monotonically and nonlinearly as D_{fr} increases from 2.0 to 3.0. A higher D_{fr} implies a more complex microscopic structure of the pore walls, which not only increases the viscous friction resistance of the flow but also significantly reduces the effective capillary driving force.

4.5.2. Effect of pore structure parameters on imbibition

To investigate the regulatory mechanisms of pore structure on imbibition behavior, five representative cases are established as illustrated in Fig. 15 and Table 3. These cases span a broad range of physical properties, ranging from high permeability in Case 1 (K = 2535.600 mD) to ultralow permeability in Case 5 (K = 0.2 mD). The maximum pore radius gradually decreases from 30 μm to 2 μm as the tortuosity and fractal dimension increase significantly. The pore size distribution frequency function of the porous media is expressed as follows [51].

$$f(R) = D_f R_{\min}^{D_f} R^{-(D_f+1)} \tag{27}$$

The permeability of the porous media is determined using the following expression [52].

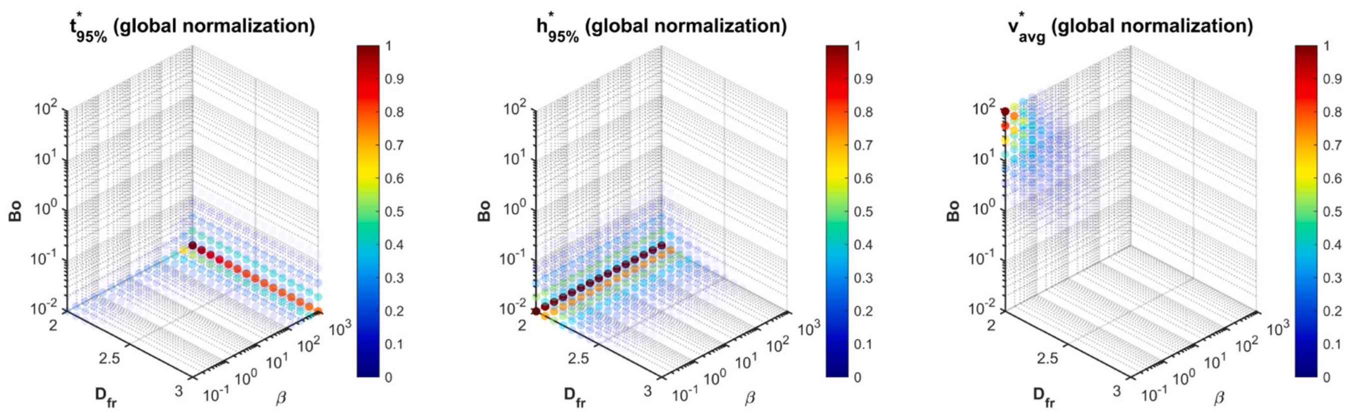
(a) Three dimensional imbibition characteristic distribution of D_{fr} - β - Bo

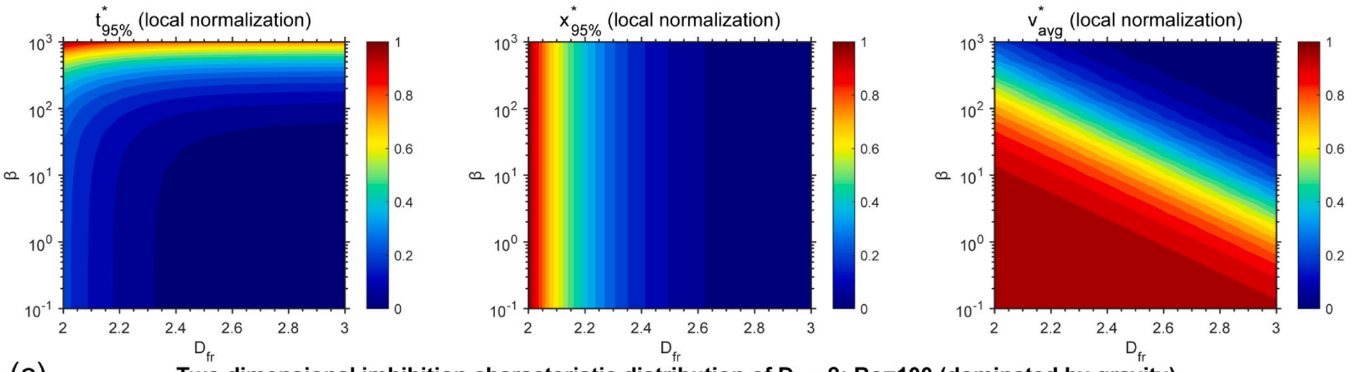
(b) Two dimensional imbibition characteristic distribution of D_{fr} - β: Bo=0.01 (dominated by capillary force)

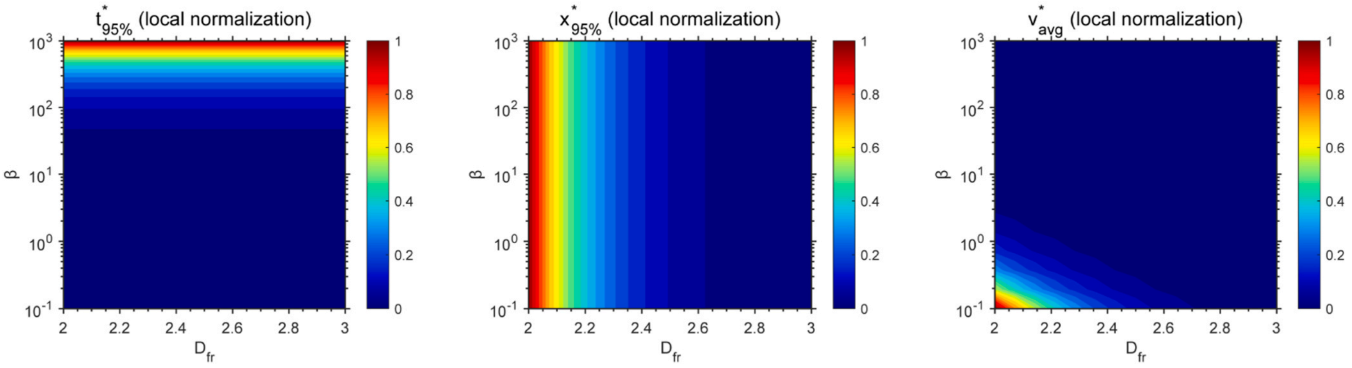
(c) Two dimensional imbibition characteristic distribution of D_{fr} - β: Bo=100 (dominated by gravity)

Fig. 13. Parameter sensitivity analysis of dimensionless imbibition characteristics ($t^*_{95\%}$, $x^*_{95\%}$ and v^*_{avg}) under different dominant mechanisms. (a) Distribution within the three-dimensional parameter space of the roughness fractal dimension D_{fr}, apparent dynamic contact angle β, and Bond number Bo. (b) Influence of D_{fr} and β on imbibition performance under the capillary-dominated condition where $Bo = 0.01$. (c) Influence of D_{fr} and β on imbibition performance under the gravity-dominated condition where $Bo = 100$. Note: To prevent data occlusion in the 3D scatter plots, the opacity of the data points is linearly mapped to their normalized values. Lower values are rendered semi-transparent to reveal the internal distribution of higher-value points.

$$K = \frac{(2 - D_f)\phi}{8\tau\left(1 - \phi\right)R_{\max}^{2-D_f}}\frac{1}{4 - D_f}R^{4-D_f}\Big|_{R_{\min}}^{R_{\max}} \tag{28}$$

Fig. 15**(a)** illustrates distinct multiscale power law characteristics in the pore size distributions across the five cases, which directly determines their fluid transport capacities. As shown in Fig. 15**(b)**, high permeability media such as Case 1 reach equilibrium within 100 s due to wide pore throats and low tortuosity. Conversely, ultralow permeability media like Case 5 are limited by nanometer scale throats and highly tortuous paths, extending the equilibrium time beyond 10^5 seconds. The sensitivity of the system to dynamic wetting effects highly depends on the pore structure. In high permeability media, the drastic inflation of the apparent dynamic contact angle θ_a causes the profiles considering dynamic effects (solid lines) to lag significantly behind those ignoring them (dashed lines). Such temporal lagging indicates that dynamic corrections are essential for accurate early stage predictions in high permeability systems. Conversely, the high intrinsic viscous resistance in low permeability cases suppresses the flow velocity and dampens the dynamic response. Under such conditions, the viscous dissipation effects governed by the pore structure occupy the dominant position. As demonstrated in recent fractal network models [27], such structural restrictions are primarily driven by increased flow tortuosity and micro-scale surface friction.

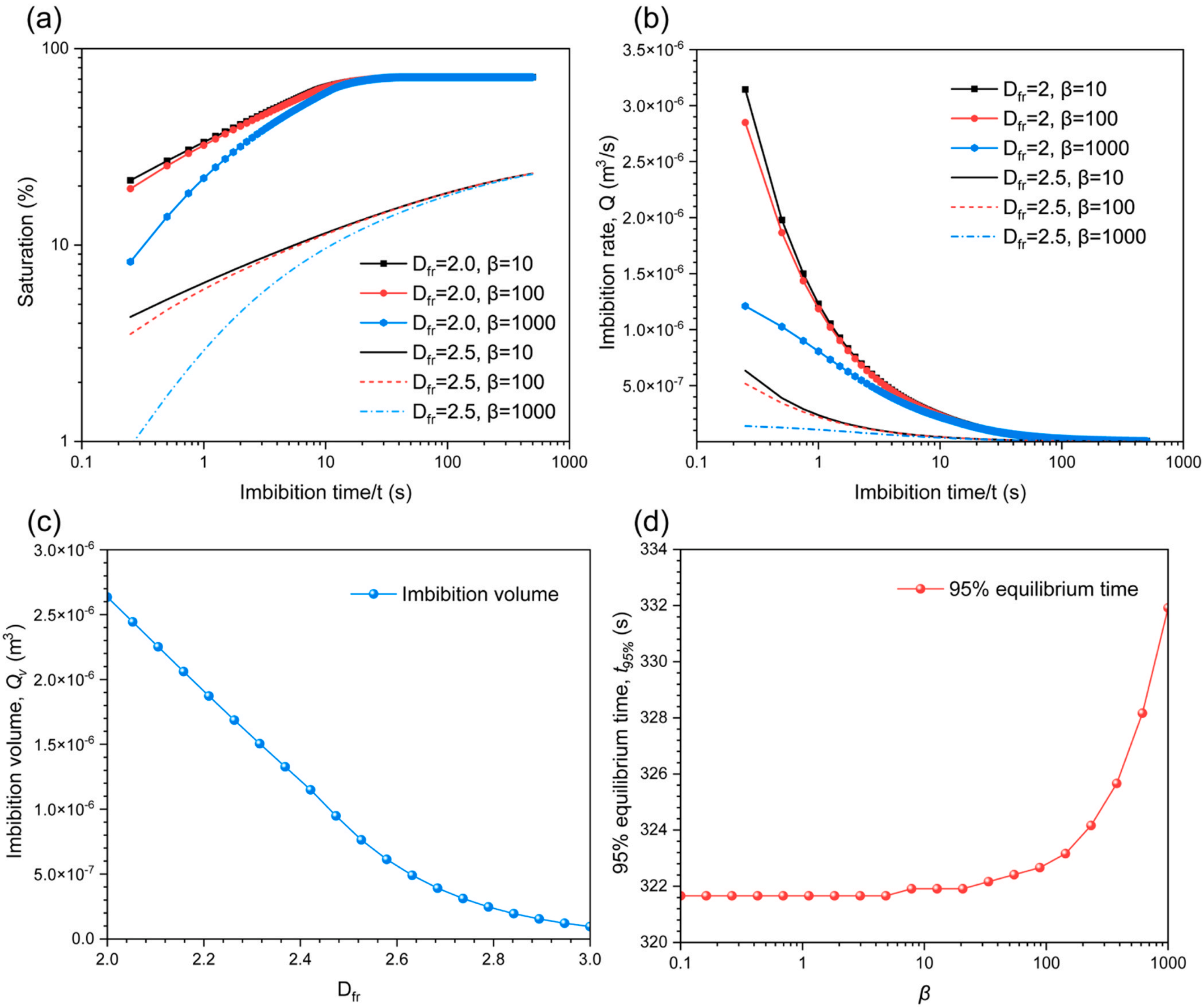

Fig. 14. Synergistic effects of the apparent dynamic contact angle β and roughness fractal dimension D_{fr} on macroscopic spontaneous imbibition characteristics under various parameter combinations. The results include (a) the evolution of saturation, (b) the evolution of the imbibition rate, (c) the sensitivity of the final imbibition volume to D_{fr}, and (d) the sensitivity of the $t_{95\%}$ to β. (The fixed simulation parameters are $\mu = 1$ mPa·s, $\rho = 1000$ kg/m^3, $\sigma = 0.072$ N/m, $\theta_S = 60^\circ$, $\alpha = 90^\circ$, $L = 5$ cm, $D_C = 2.5$ cm,$\varphi = 0.15$, $D_f = 1.85$, and $R \in [10, 1000]$ μm.).

4.5.3. Effects of fluid properties and boundary conditions on imbibition

Fig. 16 systematically analyzes the influence of pore fractal dimension D_f, static contact angle θ_s, and inclination angle α on imbibition dynamics. As shown in Figs. 16**(a)** and 16**(d)**, the imbibition rate Q decreases significantly as D_f increases from 1.65 to 1.95. This occurs because a higher D_f implies a more complex pore structure with more tortuous flow channels, where the enhanced geometric resistance substantially delays the dynamic process. This phenomenon is in accordance with the theoretical results of Zhang et al. [63], who reported that a higher fractal complexity dramatically increases local viscous dissipation and restrains the overall imbibition capacity. Furthermore, the system exhibits extreme sensitivity to wettability. Comparing Figs. 16 **(b)** and 16**(e)**, when θ_s increases from 35° to 75°, the initial imbibition rate drops sharply and the equilibrium time increases by nearly an order of magnitude. This suggests that enhancing wettability is an effective strategy for improving imbibition efficiency. Pu et al. [66] also confirmed this mechanism at the micro-scale using phase-field simulations. Figs. 16**(c)** and 16**(f)** reveal the evolutionary control mechanism of α on imbibition dynamics. However, as the fluid advances deeper, the cumulative gravitational effect gradually becomes prominent. This increasing gravitational resistance accelerates the depletion of the net driving force, forcing the high inclination system to reach mechanical equilibrium earlier and significantly suppressing the ultimate saturation, as described by the classical fractal model with gravity [16].

5. Conclusions

In this study, a unified multiscale fractal imbibition model was developed to evaluate mass transfer dynamics in complex porous media. Pore wall roughness, the dynamic contact angle, and gravitational effects were explicitly coupled within this theoretical framework. Based on the explicit analytical solution, we systematically investigated how these competing forces evolve across different scales through dimensionless analysis and multi-parameter sensitivity evaluation. The main conclusions of this study are drawn as follows:

(1) By introducing the Lambert W function, an explicit analytical solution is derived for the highly nonlinear ODE governing imbibition. This analytical solution effectively overcomes the

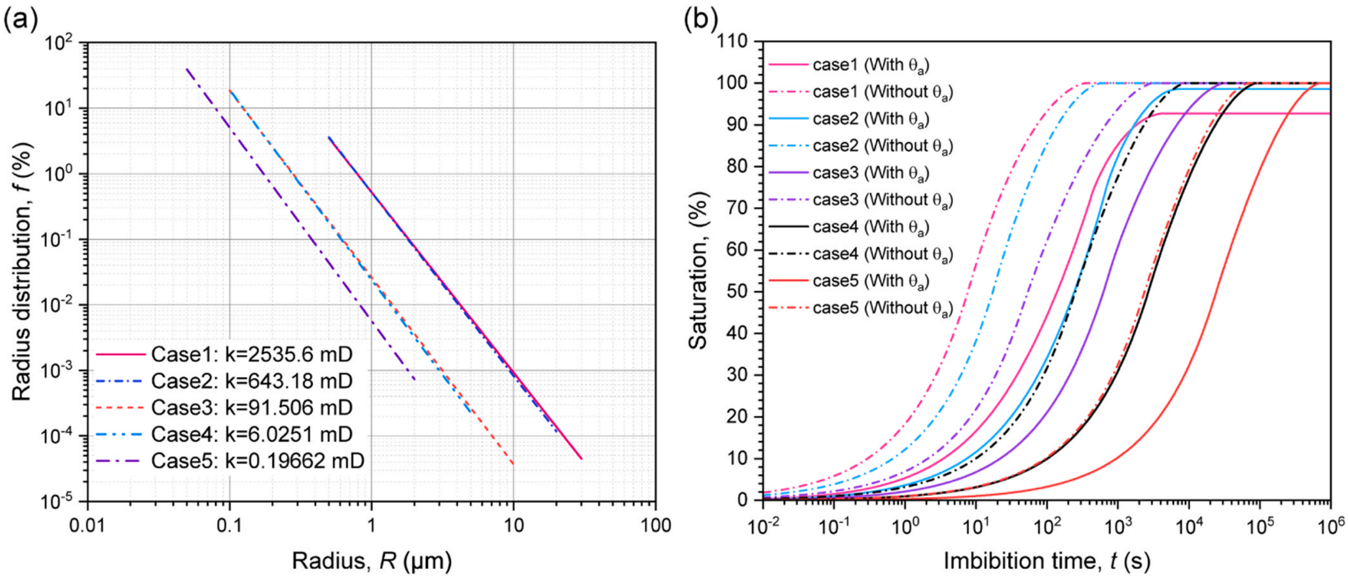

Fig. 15. Regulatory effects of the apparent dynamic contact angle θ_a on the imbibition performance of porous media with various permeabilities. (a) Pore size distribution characteristic curves for five different cases. (b) Comparison of wetting phase saturation evolution over time with and without considering the apparent dynamic contact angle. (The fixed simulation parameters are $\mu = 1$ mPa·s, $\rho = 1000$ kg/m^3, $\sigma = 0.072$ N/m, $\theta_S = 60^\circ$, $\alpha = 90^\circ$, $L = 5$ cm, $D_C = 2.5$ cm. Other fluid properties and geometric parameters are detailed in Table 3.).

Table 3
Pore structure characteristics and physical parameters of porous media across different permeability levels.

Case No.	Classification	R_{max} (μm)	R_{min} (μm)	φ (%)	D_f	τ	K (mD)
1	High Permeability	30	0.5	0.20	1.75	1.25	2535.600
2	Medium Permeability	20	0.5	0.18	1.80	1.57	643.180
3	Low Permeability	10	0.1	0.15	1.85	1.70	91.506
4	Ultra-low Permeability	5	0.1	0.10	1.90	2.78	6.025
5	Extra-low Permeability	2	0.05	0.08	1.95	5.46	0.197

time step dependence of conventional explicit solvers and the iterative convergence difficulties of implicit schemes, significantly improving computational efficiency and physical accuracy.

(2) Surface roughness induces a prominent static inhibition mechanism during imbibition. Contact line pinning on rough walls directly weakens the effective capillary driving force. This mechanism substantially lowers the final equilibrium distance, particularly in nanoscale micropores. Ultimately, extreme roughness can critically impair mass transfer capacity and transform micropores into ineffective flow channels.

(3) The dynamic contact angle acts as a nonlinear kinetic retardation mechanism. It exponentially prolongs the equilibrium time without altering the final thermodynamic equilibrium distance. While this retardation is particularly pronounced in large pores, medium-scale pores uniquely maintain the longest high-speed imbibition stage. Consequently, these intermediate pores stimulate the maximum dynamic contact angle peak.

(4) Spontaneous imbibition progresses through three distinct stages dominated by fractal roughness, dynamic wetting, and the Bond number. Dimensionless analysis reveals significant parameter decoupling. The final equilibrium distance is jointly determined by surface roughness and gravity through different mechanisms. Roughness statically reduces the capillary driving force, whereas gravity acts as a cumulative resistance along the flow path. Conversely, the equilibrium time is fundamentally controlled by dynamic wetting.

(5) The macroscopic pore structure fundamentally dictates the sensitivity of the system to apparent dynamic wetting. Neglecting apparent dynamic corrections in high permeability media leads to a severe overestimation of early stage imbibition rates. Conversely, the intrinsic viscous resistance of the pore skeleton absolutely dominates in ultra-low permeability systems, which substantially weakens the apparent dynamic wetting effect.

The proposed analytical model provides an efficient predictive tool for gas-liquid mass transfer in rough porous media, guiding subsurface energy development strategies and the targeted fabrication of porous materials. However, as an effective continuum description, it is inherently constrained by assumptions of homogeneous wettability, Wenzel-like wetting, laminar flow, and 1D independent capillary bundles. Specifically, the macroscopic Wenzel assumption requires the liquid to fully wet the rough pore walls without stable trapped gas layers, oversimplifying extreme topographies that may trigger the Cassie-Baxter state. Consequently, for real porous media involving strong contact angle hysteresis, complex topological connectivity, or heterogeneous wettability, additional corrections are required. Future work will address these limitations by extending the model to 3D interconnected networks and incorporating micro-hydrodynamic criteria for localized wetting transitions.

CRediT authorship contribution statement

Yong Kong: Writing – review & editing, Visualization, Conceptualization. **Hui Yue:** Writing – review & editing, Writing – original draft, Visualization, Methodology, Investigation, Formal analysis, Data curation, Conceptualization. **Yubiao Sun:** Writing – review & editing, Supervision, Project administration, Formal analysis, Conceptualization. **Jos Derksen:** Writing – review & editing, Supervision, Conceptualization. **Ying Li:** Validation.

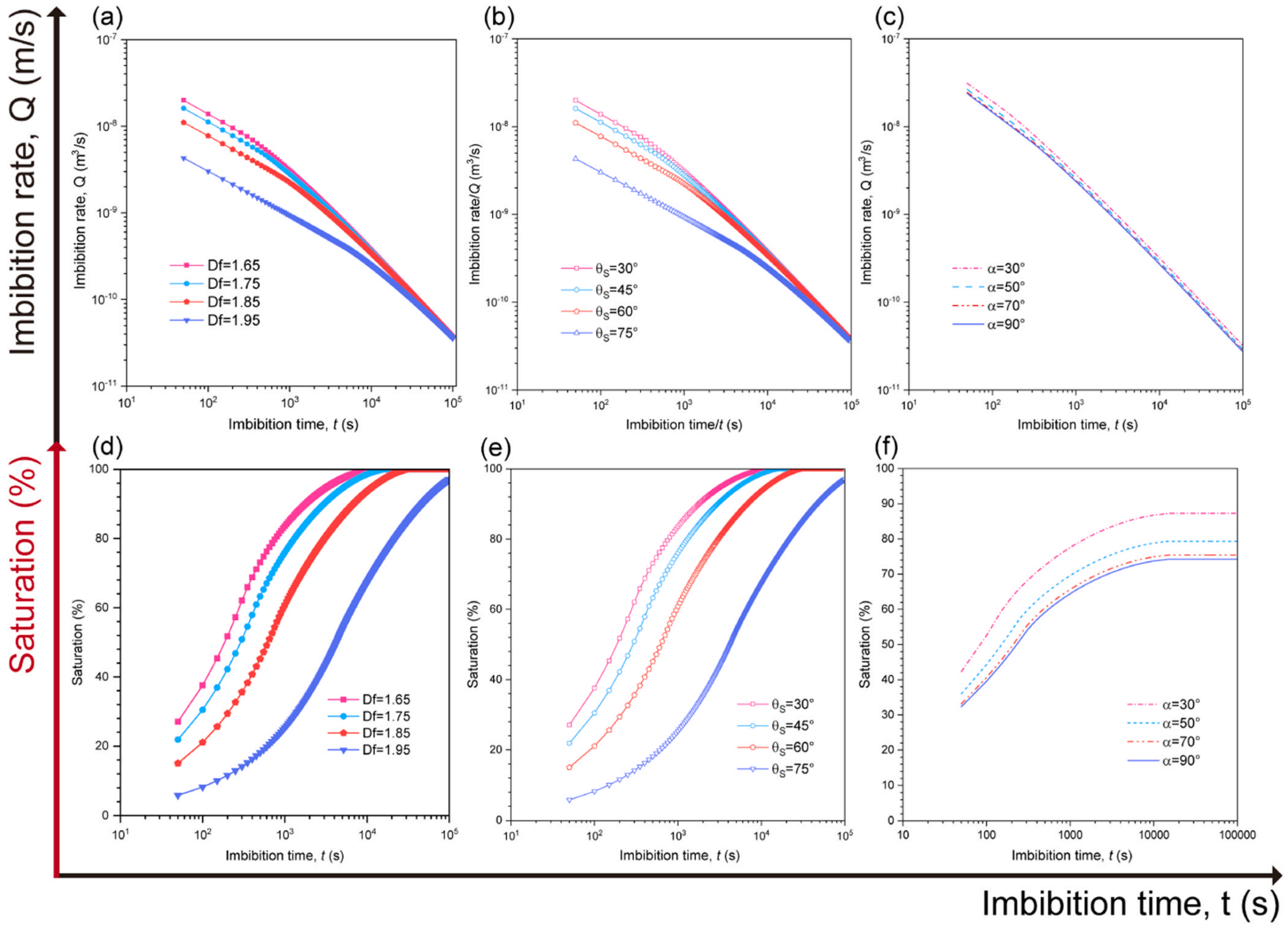

Fig. 16. Sensitivity analysis of spontaneous imbibition dynamics to key physical parameters and boundary conditions. The effects of (a) the pore fractal dimension D_f, (b) the static contact angle θ_s, and (c) the inclination angle α on the time evolution of the imbibition rate Q are presented. The corresponding evolution curves of the wetting phase saturation are shown in (d), (e), and (f).

Declaration of Competing Interest

The authors declare that they have no known competing financial interests or personal relationships that could have appeared to influence the work reported in this paper.

Appendix A. Nondimensionalization of the governing equation for a single rough capillary

To facilitate the numerical solution and theoretical analysis, this appendix details the nondimensionalization procedure for the flow model in a single rough capillary.

A.1. Dimensional governing equation

Let R and $x(t)$ denote the capillary radius and the instantaneous liquid height respectively. Based on Poiseuille law, the differential governing equation accounting for the competition among capillary force, viscous resistance, and gravity is expressed as **Eq. (A.1)**.

$$\frac{8\mu x}{R^2}\frac{dx}{dt} = \frac{2\sigma\cos\theta_a}{R} - \rho g x \sin\alpha \tag{A.1}$$

where $\cos\theta_a$ is the apparent dynamic contact angle, and its detailed derivation is provided in Section 2.1.

A.2. Selection of characteristic scales and dimensionless variables

To ensure a compact dimensionless form and facilitate comparative analysis across different physical systems, R is selected as the characteristic length L_c.

$$L_c = R \tag{A.2}$$

An analysis of the initial governing equation indicates that the capillary driving force and viscous resistance are the two core competing mechanisms dominating the early imbibition stage. Consequently, by equating these two terms at the characteristic scale to achieve mechanical equilibrium and substituting the characteristic length, the characteristic time t_c of the system is derived as **Eq. (A.3)**.

$$t_c = \frac{4\mu R}{\sigma \cos \theta_s} \tag{A.3}$$

Selecting this characteristic time not only effectively simplifies the dimensionless expression of the capillary term but also naturally transforms the dynamic contact angle effect into a dimensionless proportional coefficient. Based on these characteristic scales, the dimensionless imbibition distance x^*, dimensionless imbibition time t^*, and dimensionless imbibition velocity v^* are further defined by **Eqs. (A.4)**, **(A.5)**, and **(A.6)** respectively.

$$x^* = \frac{x}{R} \tag{A -4}$$

$$t^* = \frac{t}{t_c} \tag{A -5}$$

$$v^* = \frac{v}{v_c} = \frac{v}{R/t_c} = \frac{t_c}{R} v \tag{A -6}$$

To facilitate subsequent quantitative evaluation, based on the aforementioned fundamental dimensionless quantities, the normalized 95% equilibrium distance x^*_{95}, the normalized 95% imbibition time t^*_{95}, and the normalized average imbibition velocity v^*_{avg} are further defined by **Eqs. (A.7)**, **(A.8)**, and **(A.9)** respectively.

$$\overline{x^*_{95}} = \frac{x^*_{95} - x^*_{95,\ \min}}{x^*_{95,\ \max} - x^*_{95,\ \min}} \tag{A.7}$$

$$\overline{t^*_{95}} = \frac{t^*_{95} - t^*_{95,\ \min}}{t^*_{95,\ \max} - t^*_{95,\ \min}} \tag{A.8}$$

$$\overline{v^*_{avg}} = \frac{v^*_{avg} - v^*_{avg,\ \min}}{v^*_{avg,\ \max} - v^*_{avg,\ \min}} \tag{A.9}$$

A.3. Dimensionless treatment of the governing equation

Substituting **Eqs. (A.4)**, **(A.5)**, and **(A.6)** into the initial governing equation Eq. **(A.1)** and simplifying the terms yields Eq. (A.10).

$$x^* v^* = \frac{t_c}{8\mu} \cdot \frac{2\sigma}{R} \cos \theta_a - \frac{t_c}{8\mu} \rho g R\, x^* \tag{A.10}$$

Further substituting **Eq. (A.3)** into **Eq. (A.10)** derives **Eq. (A.11)**.

$$x^* v^* = \frac{\cos \theta_a}{\cos \theta_s} - Box^* \tag{A.11}$$

where Bo the dimensionless Bond number characterizing the ratio of gravity to the capillary force, defined as$Bo = \frac{\rho g R^2}{2\sigma \cos \theta_s}$.

Substituting **Eq. (A.6)** into the apparent dynamic contact angle model expressed as Eq. (7) in the main text yields **Eq. (A.9)**.

$$\frac{\cos \theta_a}{\cos \theta_s} = r - \frac{\beta}{4} v^* \tag{A.12}$$

where r is the wall roughness factor representing the ratio of the actual rough inner surface area to the equivalent smooth inner surface area.

Finally, substituting **Eq. (A.12)** into **Eq. (A.11)** derives the highly nonlinear dimensionless imbibition velocity governing equation expressed as **Eq. (A.13)**.

$$v^*(t^*) = \frac{r - \mathrm{Bo} x^*(t^*)}{x^*(t^*) + \beta/4} \tag{A.13}$$

A.4. Analytical solutions under two limiting cases

Based on the derived dimensionless governing equation, analytical expressions under two limiting cases are further provided. When neglecting the gravitational effect ($Bo = 0$), integrating **Eq. (A.13)** directly and substituting the initial boundary conditions yields the explicit analytical solution expressed as **Eq. (A.14)**.

$$x^*(t^*) = -\frac{\beta}{4} + \sqrt{\left(\frac{\beta}{4}\right)^2 + 2rt^*} \tag{A.14}$$

When considering the gravitational effect ($Bo \neq 0$), applying the separation of variables method to **Eq. (A.13)** and integrating yields the implicit analytical expression shown as **Eq. (A.15)**.

$$t^*(x^*) = \frac{r+(Bo\cdot\beta)/4}{Bo^2}\ln\left(\frac{r}{r-Box^*}\right) - \frac{x^*}{Bo} \tag{A.15}$$

Although deriving an explicit algebraic solution directly under this condition presents difficulties, the aforementioned implicit solution can clearly and rigorously reflect the coupled control effect of the wall roughness factor r, the dynamic contact angle coefficient β, and the gravity term Bo on the dynamic imbibition process. The evolution law of $x^*(t^*)$ can be obtained through numerical inversion to further analyze the dimensionless characteristics of the equilibrium distance and time scale. The synergistic influence mechanisms of the dimensionless parameters r, β, and Bo on imbibition dynamics have been systematically discussed in Section 4.4.

Appendix B. Derivation of the governing equation for spontaneous imbibition in a single rough capillary

This appendix details the complete derivation process of the governing equation (Eq. 10) for spontaneous imbibition in a single rough capillary.

B.1. Simplification of the fundamental flow equation

Fluid motion in micro- and nanoscale pores satisfies the conservation of momentum, which is described by the Navier-Stokes equations for an incompressible Newtonian fluid (Eq. 8):

$$\rho\left(\frac{\partial v}{\partial t} + \left(v\cdot\nabla v\right)\right) = -\nabla P_d + \mu\nabla^2 v + \rho g \tag{8}$$

where ρ is the fluid density; v is the velocity vector; t is time; P_d is the displacement pressure; μ is the dynamic viscosity; and g is the gravitational acceleration.

For a one-dimensional, steady, and fully developed laminar flow within a capillary, the inertial force terms can be neglected. In this case, the kinematic behavior of the fluid simplifies directly to the classical Poiseuille equation (Eq. 9):

$$v = \frac{R^2\Delta P}{8\mu x} \tag{9}$$

where, R is the capillary radius; ΔP is the total pressure drop within the tube; and x denotes the advancement distance of the gas-liquid interface.

B.2. Capillary force considering dynamic contact angle and fractal roughness

In a real rough capillary tube, the total driving pressure ΔP during spontaneous imbibition is composed of the effective capillary pressure P_c, the external displacement pressure P_d, and the gravity pressure drop P_g.

According to the Young-Laplace equation, the capillary pressure is expressed as:

$$P_c = \frac{2\sigma\cos\theta_a}{R} \tag{B.1}$$

To characterize the coupled effect of the dynamic contact angle and wall roughness, we have introduced the apparent dynamic contact angle model in the main text:

$$\cos\theta_a = r\cos\theta_S - \beta\frac{\mu}{\sigma}v \tag{7}$$

where r is the surface roughness factor. Introducing fractal geometry theory to characterize the actual roughness of the wall, the roughness factor r can be represented by fractal parameters as $r = (l/\Lambda)^{2-D_{fr}}$. Substituting Eq. (7) into **Eq. (B.1)** yields the effective capillary pressure accounting for the apparent dynamic contact angle effect:

$$P_c = \frac{2\sigma}{R}\left[\left(\frac{l}{\Lambda}\right)^{2-D_{fr}}\cos\theta_s - \beta\frac{\mu}{\sigma}v\right] = \frac{2\sigma\cos\theta_s}{R}\left(\frac{l}{\Lambda}\right)^{2-D_{fr}} - \frac{2\beta\mu}{R}v \tag{B.2}$$

B.3. Force balance and derivation of the final velocity

The total pressure drop is equal to the algebraic sum of the individual pressures. Assuming the angle between the capillary and the horizontal plane is α, the pressure drop generated by gravity is $P_g = \rho g x\sin\alpha$. Therefore, the total driving force can be expressed as:

$$\Delta P = P_c + \Delta P_d - P_g = \left[\frac{2\sigma\cos\theta_s}{R}\left(\frac{l}{\Lambda}\right)^{2-D_{fr}} - \frac{2\beta\mu}{R}v\right] + \Delta P_d - \rho g x\sin\alpha \tag{B.3}$$

Substituting the above expression for the total pressure drop into the Poiseuille equation (Eq. 9) yields:

$$v = \frac{R^2}{8\mu x}\left[\frac{2\sigma\cos\theta_s}{R}\left(\frac{l}{\Lambda}\right)^{2-D_{fr}} - \frac{2\beta\mu}{R}v + \Delta P_d - \rho g x\sin\alpha\right] \tag{B.4}$$

To solve for the actual advancement velocity of the interface, isolating the terms involving v on the right side of **Eq. (B.4)**, moving them to the left side, and combining like terms yields:

$$v\left(\frac{4x+\beta R}{4x}\right)=\frac{R^2}{8\mu x}\left[\frac{2\sigma\cos\theta_s}{R}\left(\frac{l}{\Lambda}\right)^{2-D_{fr}}+\Delta P_d-\rho g x\sin\alpha\right] \tag{B.5}$$

Further simplification leads to the final governing equation for spontaneous imbibition (Eq. 10):

$$v=\frac{dx}{dt}=\frac{R^2}{2\mu(4x+\beta R)}\left(\frac{2\sigma\cos\theta_s}{R}\cdot\left(\frac{l}{\Lambda}\right)^{2-D_{fr}}+\Delta P_d-\rho g x\sin\alpha\right) \tag{10}$$

Data Availability

Data will be made available on request.

References

[1] N.R. Morrow, G. Mason, Recovery of oil by spontaneous imbibition, Curr. Opin. Colloid Interface Sci. 6 (2001) 321–337, https://doi.org/10.1016/S1359-0294(01)00100-5.

[2] O.A. Simonov, Y.Y. Erina, A.A. Ponomarev, Review of modern models of porous media for numerical simulation of fluid flows, Heliyon 9 (2023) e22292, https://doi.org/10.1016/j.heliyon.2023.e22292.

[3] J. Cai, X. Qin, X. Xia, X. Jiao, H. Chen, H. Wang, Y. Xia, Numerical modeling of multiphase flow in porous media considering micro-and nanoscale effects: A comprehensive review, Gas. Sci. Eng. 131 (2024) 205441, https://doi.org/10.1016/j.jgsce.2024.205441.

[4] Y. Hao, W. Yan, Y. Su, Y. Sun, R. Liu, J. Wang, F. Yang, Gas–water two-phase displacement mechanism in fractal structure of tight sandstone gas reservoir based on nuclear magnetic resonance experiment, Phys. Fluids 37 (2025) 083118, https://doi.org/10.1063/5.0280742.

[5] G. Li, Y. Su, W. Wang, The fractal mathematical models for spontaneous and forced imbibition with different cross-section shapes in shale oil reservoir, Fractals 31 (2023) 2350002, https://doi.org/10.1142/S0218348×23500020.

[6] H. Cheng, F. Wang, G. Yang, X. Guan, Z. Cheng, H. Li, C. Yu, G. Feng, Y. Yuan, Prediction of relative permeability from capillary pressure based on the fractal capillary bundle model, Appl. Therm. Eng. 239 (2024) 122093, https://doi.org/10.1016/j.applthermaleng.2023.122093.

[7] S.A.F. Abad, A. Hassanpouryouzband, K. Edlmann, M. Wilkinson, R.S. Haszeldine, Capillary trapping in cyclic injection and withdrawal for geological hydrogen storage, J. Energy Storage 153 (2026) 120987, https://doi.org/10.1016/j.est.2026.120987.

[8] X. Liang, Y. Yang, H. Li, Q. Zhang, Y. Li, H. Sun, L. Zhang, J. Zhong, K. Zhang, J. Yao, Interfacial wettability evolution in underground hydrogen storage: Key factors, multiscale effects, and challenges, Adv. Colloid Interface Sci. (2025) 103763, https://doi.org/10.1016/j.cis.2025.103763.

[9] G. Zhang, Z. Qu, W. Tao, X. Wang, L. Wu, S. Wu, X. Xie, C. Tongsh, W. Huo, Z. Bao, Porous flow field for next-generation proton exchange membrane fuel cells: materials, characterization, design, and challenges, Chem. Rev. 123 (2022) 989–1039, https://doi.org/10.1021/acs.chemrev.2c00539.

[10] J. Cai, B. Yu, M. Zou, L. Luo, Fractal characterization of spontaneous co-current imbibition in porous media, Energy Fuels 24 (2010) 1860–1867, https://doi.org/10.1021/ef901413p.

[11] Y. Zhou, S. Wu, R. Zhu, X. Jiang, G. Hua, A new model for determining the effective permeability of tight reservoirs based on Fractal-Monte Carlo method, Pet. Sci. 22 (2025) 3101–3118, https://doi.org/10.1016/j.petsci.2025.04.016.

[12] R. Lucas, Rate of capillary ascension of liquids, Kolloid Z 23 (1918) 15–22, https://doi.org/10.1007/bf01461107.

[13] E.W. Washburn, The dynamics of capillary flow, Phys. Rev. 17 (1921) 273, https://doi.org/10.1103/PhysRev.17.273.

[14] C.W. Nutt, The physical basis of the displacement of oil from porous media by other fluids: a capillary bundle model, Proc. R. Soc. Lond. Proc. R. Soc. Lond. A 382 (1982) 155–178, https://doi.org/10.1098/rspa.1982.0094.

[15] K.G. Kornev, A.V. Neimark, Modeling of spontaneous penetration of viscoelastic fluids and biofluids into capillaries, J. Colloid Interface Sci. 262 (2003) 253–262, https://doi.org/10.1007/bf01461107.

[16] J. Cai, X. Hu, D.C. Standnes, L. You, An analytical model for spontaneous imbibition in fractal porous media including gravity, Colloids Surf. A 414 (2012) 228–233, https://doi.org/10.1016/j.colsurfa.2012.08.047.

[17] F. Wang, J. Zhao, Mathematical modeling of gravity and buoyancy effect on low interfacial tension spontaneous imbibition in tight oil reservoirs, AIChE J. 67 (2021) e17332, https://doi.org/10.1002/aic.17332.

[18] J. Cai, B. Yu, A discussion of the effect of tortuosity on the capillary imbibition in porous media, Transp. Porous Media 89 (2011) 251–263, https://doi.org/10.1007/s11242-011-9767-0.

[19] J. Cai, E. Perfect, C. Cheng, X. Hu, Generalized modeling of spontaneous imbibition based on Hagen–Poiseuille flow in tortuous capillaries with variably shaped apertures, Langmuir 30 (2014) 5142–5151, https://doi.org/10.1021/la5007204.

[20] Z. Zhao, Z. Jiang, J. Guo, S. He, C. Chen, A new multi-pore fractal model to delineate the effect of various factors on imbibition in shales, Fuel Commun. 7 (2021) 100012, https://doi.org/10.1016/j.jfueco.2021.100012.

[21] B. Yu, Analysis of flow in fractal porous media, Appl. Mech. Rev. 61 (2008) 050801, https://doi.org/10.1115/1.2955849.

[22] B. Hu, J. Wang, Z. Ma, S. Sang, Permeability and thermal conductivity models of shale matrix with a bundle of tortuous fractal tree-like branching micropore networks, Int. J. Therm. Sci. 164 (2021) 106876, https://doi.org/10.1016/j.ijthermalsci.2021.106876.

[23] S. Yang, M. Liang, B. Yu, M. Zou, Permeability model for fractal porous media with rough surfaces, Microfluid. Nanofluid 18 (2015) 1085–1093, https://doi.org/10.1007/s10404-014-1500-1.

[24] Q. Zheng, J. Fan, X. Li, C. Xu, Fractal analysis of the effect of rough surface morphology on gas slip flow in micro-and nano-porous media, Chem. Eng. Sci. 189 (2018) 260–265, https://doi.org/10.1016/j.ces.2018.05.065.

[25] Y. Zeng, B. Ji, Y. Zhang, J. Feng, J. Luo, M. Wang, A fractal model for effective thermal conductivity in complex geothermal media, Front. Earth Sci. 10 (2022) 786290, https://doi.org/10.3389/feart.2022.786290.

[26] A. Shen, Y. Liu, S.F. Ali, A model of spontaneous flow driven by capillary pressure in nanoporous media, Capillarity 3 (2020) 1–7, https://doi.org/10.46690/capi.2020.01.01.

[27] T. Xiao, J. Guo, G. Liu, X. Yang, T.J. Lu, An analytical fractal model for permeability in isotropic open-cell metal foam with surface roughness, Int. Commun. Heat. Mass. Transf. 126 (2021) 105473, https://doi.org/10.1016/j.icheatmasstransfer.2021.105473.

[28] S. Yang, R. Cui, J. Liu, M. Wang, L. Gao, Fractal study of interporosity flow function and shape factor in rough fractured dual porous media, Chem. Eng. Sci. 280 (2023) 118960, https://doi.org/10.1016/j.ces.2023.118960.

[29] G. Li, Y. Yang, X. Cao, S. Zhang, Q. Lv, Y. Su, W. Wang, The fractal analysis of the forced imbibition process in roughened porous media with slip length, Phys. Fluids 37 (2025) 046603, https://doi.org/10.1063/5.0244581.

[30] S. Yang, Q. Sheng, M. Zou, Q. Zheng, The influence of gravity on the fractal model of imbibition in rough pores considering shape factor, Chin. J. Phys. 96 (2025) 1261–1271, https://doi.org/10.1016/j.cjph.2025.06.034.

[31] M. Hilpert, Effects of dynamic contact angle on liquid withdrawal from capillary tubes:(Semi)-analytical solutions, J. Colloid Interface Sci. 347 (2010) 315–323, https://doi.org/10.1016/j.jcis.2010.03.055.

[32] F. Wang, J. Zhao, Mathematical model of liquid spontaneous imbibition into gas-saturated porous media with dynamic contact angle and gravity, Chem. Eng. Sci. 229 (2021) 116139, https://doi.org/10.1016/j.ces.2020.116139.

[33] M.J. Blunt, B. Bijeljic, H. Dong, O. Gharbi, S. Iglauer, P. Mostaghimi, A. Paluszny, C. Pentland, Pore-scale imaging and modelling, Adv. Water Resour. 51 (2013) 197–216, https://doi.org/10.1016/j.advwatres.2012.03.003.

[34] Y. Yang, J. Wang, J. Wang, Q. Zhang, J. Yao, Pore-scale numerical simulation of supercritical CO_2-brine two-phase flow based on VOF method, Nat. Gas. Ind. 10 (2023) 466–475, https://doi.org/10.1016/j.ngib.2023.08.002.

[35] C. Cuttle, C.W. MacMinn, Dynamics of compression-driven gas-liquid displacement in a capillary tube, Phys. Rev. Lett. 130 (2023) 114001, https://doi.org/10.1103/PhysRevLett.130.114001.

[36] Z. Sun, B. Zhang, Q. Liu, L. Xu, A pore-scale investigation of flow patterns during spontaneous and forced imbibition in fractured porous media, Phys. Fluids 36 (2024) 126632, https://doi.org/10.1063/5.0245799.

[37] X. Qin, H. Wang, Y. Xia, W. He, X. Xia, J. Cai, Three-dimensional modeling of nanoconfined multiphase flow in clay nanopores using FIB-SEM images of shale, Innov. Energy 1 (2024) 100050, https://doi.org/10.59717/j.xinn-energy.2024.100050.

[38] Y. Yang, W. He, G. Lu, S. Wang, Z. Liu, H. Wang, Lattice Boltzmann simulation of oil–water forced imbibition in multi-scale pore structure, Phys. Fluids 37 (2025) 062008, https://doi.org/10.1063/5.0268352.

[39] J. Mo, C. Zhang, W. Zheng, Y. Hu, Z. Li, T. Suekane, Influence of binder content on gas-water two-phase flow and displacement phase diagram in the gas diffusion layer of PEMFC: A pore network view, Int. J. Heat. Mass. Transf. 231 (2024) 125838, https://doi.org/10.1016/j.ijheatmasstransfer.2024.125838.

[40] S.M. Hassanizadeh, W.G. Gray, Thermodynamic basis of capillary pressure in porous media, Water Resour. Res. 29 (1993) 3389–3405, https://doi.org/10.1029/93WR01495.

[41] M. Ebadi, J. McClure, P. Mostaghimi, R.T. Armstrong, Bridging the gap: Connecting pore-scale and continuum-scale simulations for immiscible multiphase flow in

porous media, Phys. Fluids 36 (2024) 033305, https://doi.org/10.1063/5.0186990.

[42] J.W. Brabazon, E. Perfect, C.H. Gates, L.J. Santodonato, I. Dhiman, H.Z. Bilheux, J. Bilheux, L.D. McKay, Spontaneous imbibition of a wetting fluid into a fracture with opposing fractal surfaces: Theory and experimental validation, Fractals 27 (2019) 1940001, https://doi.org/10.1142/S0218348×19400012.

[43] A. Majumdar, C.L. Tien, Fractal characterization and simulation of rough surfaces, Wear 136 (1990) 313–327, https://doi.org/10.1016/0043-1648(90)90154-3.

[44] F. Family, T.S. Vicsek, Dynamics of fractal surfaces, World Scientific,, 1991.

[45] E. Perfect, J.W. Brabazon, C.H. Gates, Forward prediction of early-time spontaneous imbibition of water in unsaturated rock fractures, Vadose Zone J. 19 (2020) e20056, https://doi.org/10.1002/vzj2.20056.

[46] R.N. Wenzel, Resistance of solid surfaces to wetting by water, Ind. Eng. Chem. 28 (1936) 988–994, https://doi.org/10.1021/ie50320a024.

[47] T.D. Blake, The physics of moving wetting lines, J. Colloid Interface Sci. 299 (2006) 1–13, https://doi.org/10.1016/j.jcis.2006.03.051.

[48] M.R. Stukan, P. Ligneul, J.P. Crawshaw, E.S. Boek, Spontaneous imbibition in nanopores of different roughness and wettability, Langmuir 26 (2010) 13342–13352, https://doi.org/10.1021/la101995t.

[49] D. Bonn, J. Eggers, J. Indekeu, J. Meunier, E. Rolley, Wetting and spreading, Rev. Mod. Phys. 81 (2009) 739–805, https://doi.org/10.1103/RevModPhys.81.739.

[50] Y. Tsunazawa, T. Yokoyama, N. Nishiyama, An experimental study on the rate and mechanism of capillary rise in sandstone, Prog. Earth Planet. Sci. 3 (2016) 8, https://doi.org/10.1186/s40645-016-0086-5.

[51] B. Yu, J. Li, Some fractal characters of porous media, Fractals 9 (2001) 365–372, https://doi.org/10.1142/S0218348×01000804.

[52] F. Wang, J. Zhao, A mathematical model for co-current spontaneous water imbibition into oil-saturated tight sandstone: Upscaling from pore-scale to core-scale with fractal approach, J. Pet. Sci. Eng. 178 (2019) 376–388, https://doi.org/10.1016/j.petrol.2019.03.055.

[53] G. Li, Y. Su, W. Wang, Q. Sun, Mathematical model and application of spontaneous and forced imbibition in shale porous media-considered forced pressure and osmosis, Energy Fuels 36 (2022) 5723–5736, https://doi.org/10.1021/acs.energyfuels.2c00680.

[54] P. Huber, S. Gruener, C. Schäfer, K. Knorr, A.V. Kityk, Rheology of liquids in nanopores: A study on the capillary rise of water, n-Hexadecane and n-Tetracosane in mesoporous silica, Eur. Phys. J. Spec. Top. 141 (2007) 101–105, https://doi.org/10.1140/epjst/e2007-00024-0.

[55] O.A. Olafuyi, Y. Cinar, M.A. Knackstedt, W.V. Pinczewski, Spontaneous Imbibition in Small Cores, SPE Asia Pacific Oil and Gas Conference and Exhibition, Jakarta, Indonesia, 2007, Paper No. SPE-109724-MS. 〈https://doi.org/10.2118/109724-MS〉.

[56] N. Fries, M. Dreyer, An analytic solution of capillary rise restrained by gravity, J. Colloid Interface Sci. 320 (2008) 259–263, https://doi.org/10.1016/j.jcis.2008.01.009.

[57] B.V. Zhmud, F. Tiberg, K. Hallstensson, Dynamics of capillary rise, J. Colloid Interface Sci. 228 (2000) 263–269, https://doi.org/10.1006/jcis.2000.6951.

[58] R.L. Hoffman, A study of the advancing interface. I. Interface shape in liquid—gas systems, J. Colloid Interface Sci. 50 (1975) 228–241, https://doi.org/10.1016/0021-9797(75)90225-8.

[59] H. Šikalo, I.V. Wilhelm, S. Roisman, C. Jakirlić, Tropea, Dynamic contact angle of spreading droplets: Experiments and simulations, Phys. Fluids 17 (2005) 062103, https://doi.org/10.1063/1.1928828.

[60] D. Quéré, Wetting and roughness, Annu. Rev. Mater. Res. 38 (2008) 71–99, https://doi.org/10.1146/annurev.matsci.38.060407.132434.

[61] P.M. Garcia Eijo, J.M. Cabaleiro, G. Artana, Capillary flow dynamics in composite rectangular microchannels with rough walls, Langmuir 38 (2022) 13296–13304, https://doi.org/10.1021/acs.langmuir.2c02496.

[62] M. Kadivar, D. Tormey, G. McGranaghan, CFD of roughness effects on laminar heat transfer applied to additive manufactured minichannels, Heat. Mass. Transf. 60 (2024) 1915–1929, https://doi.org/10.1007/s00231-022-03268-1.

[63] L. Zhang, G. Imani, L. Kang, J. Ping, H. Sun, D. Fan, S. Fu, L. Hou, B.S. Memon, Y. Yang, Fractal theory and dynamic contact angle-based imbibition model for two-phase flow in porous media, Phys. Fluids 35 (2023) 122019, https://doi.org/10.1063/5.0181498.

[64] N. Wang, F. Lai, Y. Fu, Z. Li, Q. Wang, Coupling the dynamic contact angle into the dynamic imbibition model for fractal porous media, Energy Fuels 37 (2023) 7201–7212, https://doi.org/10.1021/acs.energyfuels.3c00887.

[65] Y. Pu, E. Yang, D. Wang, Microscopic effect of mixed wetting capillary characteristics on spontaneous imbibition oil recovery in tight reservoirs, Energies 18 (2025) 324, https://doi.org/10.3390/en18020324.